Direct Imaging Search for Extrasolar Planets in the Pleiades Cluster

Kodai Yamamoto

February 2014

A dissertation for the degree of Doctor of Philosophy

Department of Earth and Space Science,
Graduate School of Science, Osaka University, 1-1,
Machikaneyama-cho, Toyonaka, Osaka 560-0043, Japan.

Abstract

We conducted an imaging survey of extrasolar planets around stars in the Pleiades (125 Myr, 135 pc) in the H and $K_{\rm S}$ bands using HiCIAO combined with the adaptive optics, AO188, on the Subaru telescope. We found 15 companion candidates around 10 stars, seven of which were confirmed as background stars by measuring their proper motion. Among the remaining candidates, one was absent in the second epoch observation, excluding it as a background or companion object. Another appeared in multi-epoch images, but with insufficiently precise proper motion to confirm it as a background object. One candidate might be a stellar mass ($\sim 0.6\ M_{\odot}$) companion orbiting HD 23247 (F3). Two were confirmed as 60 $M_{\rm J}$ brown dwarf companions orbiting around HD 23514 (G0) and HII 1348 (K5), as reported in previous studies. The final two candidates were co-moving companions around V1174 Tau. Their H magnitudes are 18.0 and 18.5consistent with brown dwarf masses. If confirmed, these companions are the lowest-mass companions yet identified in the Pleiades cluster. In our observations, the average detection limit for a point source was 20.6 mag in the H band beyond $1''.5$ from the central star. On the basis of this detection limit, the detection efficiency for a planet with 9–13 Jovian masses and a semi-major axis of 50–1000 AU was colculated as 80%. We then extrapolated the distribution of planet masses and semi-major axes derived from RV observations and adopted the planet evolution model of Baraffe et al. (2003). Since no planets were detected, we estimated the frequency of such planets as less than 17.5% (2σ) around single stars in the Pleiades cluster.

This study was published in *PUBLICATIONS OF THE ASTRONOMICAL SOCIETY OF JAPAN, Vol. 65, No. 4* (Yamamoto et al. 2013).

Contents

List of Figures

List of Tables

Chapter 1

Introduction

Since the discovery of an extrasolar planet around a main-sequence star in 1995 (Mayor & Queloz 1995), over 1000 extrasolar planets have been discovered by various methods. The masses of planets discovered to date are plotted against their semi-major axes in Figure 1.1.

As shown in the figure, different methods detect planets in different regions of the planet mass versus semi-major axis diagram. These methods are detailed in Section 1.1.1–1.1.4. The implications of this diagram for planet-forming theories and the frequency of planet types are discussed in Section 1.2 and 1.3, respectively.

This study focuses on very low mass stars, such as brown dwarfs and extrasolar planets. The minimum hydrogen-burning mass of such objects is 72 $M_{\rm J}$ (Chabrier & Baraffe 2000) and their minimum deuterium-burning mass is 13.1 $M_{\rm J}$ (Saumon et al. 1996). In this paper, brown dwarfs and planets are considered as stars of deuterium-burning mass 13–72 $M_{\rm J}$ and companions of mass below 13 $M_{\rm J}$, respectively.

1.1 Detection methods of extrasolar planets

1.1.1 Radial velocity

The first planetary mass companion orbiting a main-sequence star, named 51 Peg b, was detected by the radial velocity (RV) method in 1995 (Mayor & Queloz 1995). In fact, the RV method has detected most of the 530 planets discovered to date[1] (indicated by the green symbols in Figure 1.1).

[1] Taken from the extrasolar planet catalogue by Rein (2012); http://www.openexoplanetcatalogue.com/

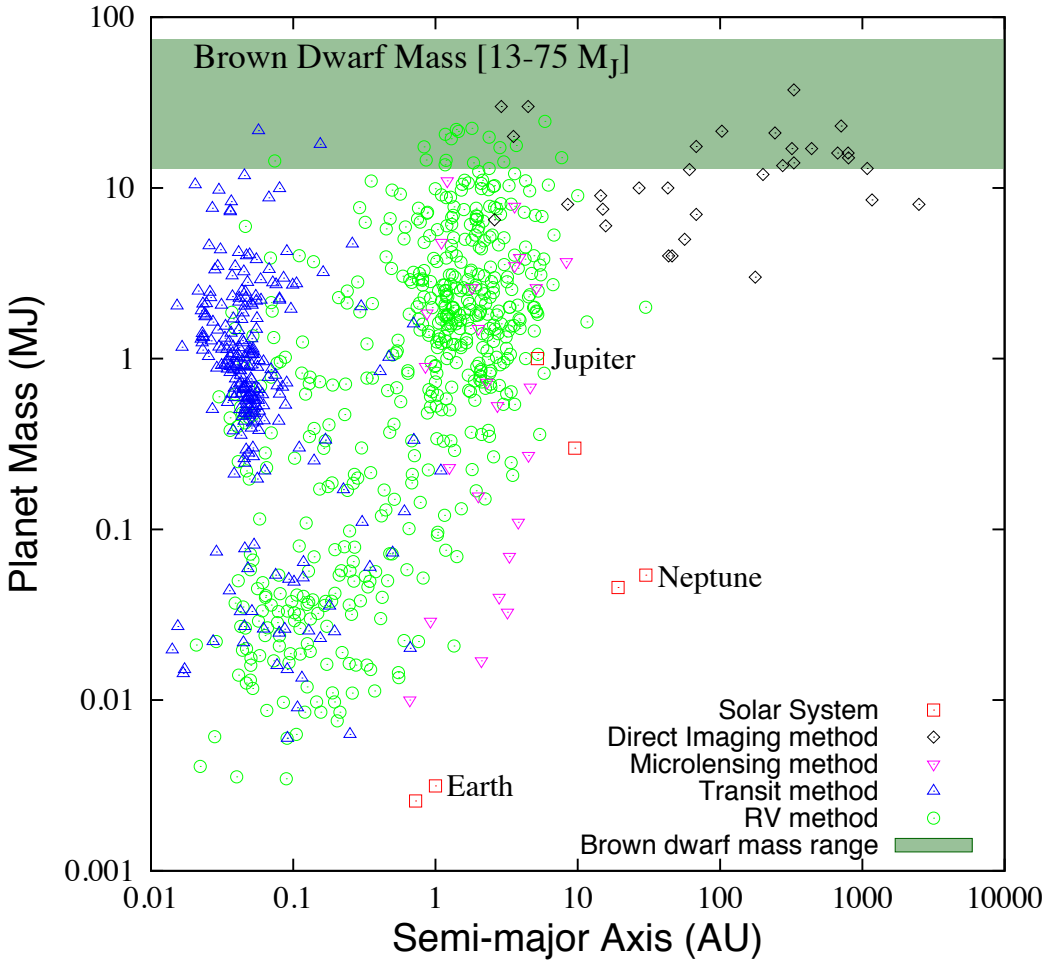

FIGURE 1.1: Mass of planets versus their semi-major axis,compliled from *The Open Exoplanet Catalogue*[1]. Discovery method is indicated by color. Details are described in Sections 1.1.1–1.1.4. Planets in the solar system are indicated by red symbols. The mass and semi-major axis of Earth is $3.14 \times 10^{-3} M_{\rm J}$ and $1.0 AU$, respectively, where $1 M_{\rm J}$ is Jupiter's mass. The semi-major axis of Jupiter is $5.2 AU$. By contrast, the mass and semi-major axis of Neptune is 5.40×10^{-2} $M_{\rm J}$ and $30 AU$, respectively.

Planetary motions induce radial motion of their central star. The component of stellar radial velocity in the line of sight can be precisely measured by Doppler shift. The variation of radial velocities reveals the period, distance and shape of the planetary orbit. From these parameters, the minimum mass ($M_P \sin i$) of the orbiting planet is given by (Wright & Gaudi 2013)

$$\frac{PK^3 (1-e^2)^{\frac{2}{3}}}{2\pi G} = \frac{M_P^3 \sin^3 i}{(M_P + M_*)}, \tag{1.1}$$

where $M_{\rm P}$ and M_* are the massesof planet and star, respectively, i is orbit inclination. P is the orbital period, K is the semi-amplitude of the signal in units of velocity, e is the eccentricity, and G is Newton's gravitational constant. According to Equation 1.1, the signal amplitude decreases as P increases and $M_{\rm P}$ reduces. When a Jupiter-mass planet circularly orbits a Solar-mass star over a period of 11.8 years, K is $\simeq 12.5 \sin i$ m/s. To achieve $K/c \sim 10^{-8}$, the RV measurement must be extremely precise, limiting the maximum semi-major axis in Figure 1.1 to ~ 10 AU. On the other hand, close-in giant planets (hot Jupiters; semi-major axis ~ 0.04 AU, period $\sim$ a few days) are typically found at intermediate distances (~ 0.1 AU) from their host stars. To ensure high accuracy spectroscopic measurements, the host star is preferably a late-G to early-F type quiet main-sequence star.

1.1.2 Transit

Planetary presence causes variations in the flux of a star system. The detection of planets by flux variation is called *transit*. The first transit planet HD 209458 b was detected by Charbonneau et al. (2000); Henry et al. (2000); Mazeh et al. (2000). Planets discovered by the transit method are indicated by the blue triangles in Figure 1.1 (~ 250 discovered[1]).

As the planet transits in front of its host star, the system flux decreases. The depth of darkening is proportional to the ratio of the projected areas of star and planet, equivalently, to the square of the ratio of the planet and star radii ($R_{\rm P}/R_*$). The orbital period is inferred from the duration of the transit and the time interval between the first and the next event. Combined with the RV method, the transit method yields the $M_{\rm P}$. Moreover, the planet density $\rho_{\rm P}$ is derivable from $M_{\rm P}$ and $R_{\rm P}$. When the transiting planet disappears behind its host star, the flux similarly decreases because the planet's contribution is lost. This passage, called the secondary eclipse, enables the planet flux to be measured from the depth of the darkening. If the secondary eclipse is observed with sufficiently sensitive, high resolution spectroscopy, the planet radius can be determined at each wavelength. Radial variations among wavelengths are related to the constituents of the planetary atmosphere (*e.g.*, Bean et al. 2010; Narita et al. 2013). In addition, by observing the Doppler shift during the transit, the projected stellar spin-obit angle can be determined through the Rossiter–McLaughlin effect (*e.g.*, Winn et al. 2005).

The probability of transit occurrence $P_{\rm tr}$ is given by

$$P_{\rm tr} = \left(\frac{R_* + R_{\rm P}}{a}\right) \frac{1 + e\sin\omega_*}{1 - e^2}, \tag{1.2}$$

where a is the semi-major axis and ω_* is the longitude of the periastron of the star. When $R_{\rm P}/R_* \ll 1$, $P_{\rm tr} = R_*/a$. The transit probability of a typical hot Jupiter with $P \sim 3$ days ($R_{\rm P} \simeq R_{\rm J}$) is approximately 10%.

The occurrence rate of transit is low, and this method more sensitively detects close-in planets as compared to the RV method. However, high-precision photometry can simultaneously search multiple stars for planetary companions. High-precision photometry is achievable by transit space missions, which are free from fluctuations induced by the Earth's atmosphere. The space telescope *Kepler*, which searches for habitable planets, has detected over 2,300 planet candidates to date (Batalha et al. 2013). As elaborated in Section 1.3, the RV combined with the transit method is a powerful approach for investigating the frequency of close-in planets (within a few AU of their host star).

1.1.3 Microlensing

When an object (lens) passes in front of another object (source) that is in the same line of sight, the source geometry is transformed by the gravitational lensing effect. *Microlensing* increase the brightness of the source at low resolution (for example, when the source and lens lie far from the Earth and/or the lens is of low mass). If the lens comprises a star–planet system, microlensing may detect the signal caused by the planet. The 24 planets[1] detected by microlensing are indicated by the magenta triangles in Figure 1.1.

The typical scale of microlensing events is evaluated by the Einstein ring radius $r_{\rm E}$

$$r_{\rm E} \simeq 2.85AU \left(\frac{M_*}{0.5M_\odot}\right)^{1/2} \left(\frac{d_s}{8{\rm kpc}}\right) \left[\frac{x(1-x)}{0.25}\right]^{1/2}, \tag{1.3}$$

where d and d_s are the distances from Earth to the lens and source, respectively, and $x \equiv d/d_s$. Microlensing is suitable for detecting planets near the Einstein ring radius (Dong et al. 2006). As such, it detects planets around the snow line (ice boundary $a_{ice} = 2.7(M_*/M_\odot)^2 AU$; Ida & Lin 2005) with high efficiency. As shown in Figure 1.1, microlensing planets have intermediate semi-major axes ($\sim$ 0.5–10 AU). This method is also sensitive to free floating planets(Sumi et al. 2011).

However, microlensing events are rare, occurring at a rate $\Gamma \simeq 10^{-5}$ event per star per year (Kiraga & Paczynski 1994; Sumi et al. 2013). In addition, planetary microlensing events are of short duration (duration time $\Delta t_p \sim 1$ day and $\Delta t_p \sim 1.5$ hours for Jovian and Earth masses, respectively), and are observed only once. Therefore, several dozen million target stars in the Galactic bulge are currently being monitored for microlensing events 24 h every day.

1.1.4 Direct imaging

Planets are most simply and straightforwardly detected by thermal processes and/or photon scattering from the planet surface. The black squares in Figure 1.1 indicate the 32 planets[1] discovered by direct imaging (DI).

It is difficult to decide which planet was the first to be detected by direct imaging. The first planetary mass object detected by direct imaging, 2M1207 b (4–10 $M_{\rm J}$; Chauvin et al. 2004; Mohanty et al. 2007), exhibited common proper motion with its host star, a brown dwarf of spectral type M8. A planetary mass object (6–13 $M_{\rm J}$; Lagrange et al. 2009, 2010) orbiting main-sequence star (A6) β Pic was predicted by analyzing the debris disk structure (*e.g.*, Freistetter et al. 2007; Mouillet et al. 1997; Okamoto et al. 2004) . Four planetary mass companions have been identified around the main-sequence star HR 8799 (A5) (Marois et al. 2008, 2010; Metchev et al. 2009). However, direct imaging of planets is limited by two difficulties. First is determining when a planet has been discovered. Second, the masses of planets discovered by direct imaging are estimated from their luminosities, some of which are based on luminosity evolution theories (detailed in Section 2.1.1). Briefly, more luminous planets are assumed to be younger and massive than their non-luminous counterparts. In addition, the accuracy of the estimated mass depends on the precision of the photometry and age estimation, because different evolution theories predict different results. The mass of most planetary objects is $< 13 M_{\rm J}$, while that of brown dwarfs is 13–72 $M_{\rm J}$.

Direct imaging detects plants that have a relatively larger (projected) semi-major axis (> 10 AU), as compared with those detected by other methods (Section 1.1.1–1.1.3), but with small separation between the planet and its host star ($< 1''$). Planets around a stars can be detected in three main ways: (1) resolving images of a planet and its host star, (2) detecting planetary flux, and (3) distinguishing the flux of a planet from that of its host star. Regarding (1), the spatial resolution of an image θ is given by $\theta \sim \lambda/D$, where D is the diameter of the telescope. The resolution of the Subaru telescope in the H-band (1.6 μm) is about

0″.05. Regarding (3), the flux ratio of reflected light between the planet and its host star $f_{ref,\lambda}$ is calculated as

$$f_{ref,\lambda} = A_{g,\lambda} \left(\frac{R_P}{a} \right)^2 \Phi_{ref,\lambda}(\alpha), \tag{1.4}$$

where $A_{j,\lambda}$ is the monochromatic geometric albedo, and $\Phi_{ref,\lambda}$ is the reflected light phase curve, which depends on the planetary phase angle α and the wavelangth λ. The reflected flux ratio of a 1 $R_{\rm J}$ planet at 10 AU is about 10^{-9}. Assuming that the planet behaves as a blackbody, the flux ratio of thermal light $f_{therm,\lambda}$ is given by

$$\begin{aligned} f_{therm,\lambda} &= \left(\frac{R_P}{R_*} \right)^2 \frac{B_\lambda(T_P)}{B_\lambda(T_*)} \Phi_{therm,\lambda}(\alpha) \\ &\rightarrow \left(\frac{R_P}{R_*} \right)^2 \frac{T_P}{T_*} \Phi_{therm,\lambda}(\alpha) \, \text{if} \, \lambda \gg \frac{hc}{k_{\rm B} T}, \end{aligned} \tag{1.5}$$

where $\Phi_{therm,\lambda}(\alpha)$ is the monochromatic thermal phase curve. If the effective temperatures of the young (< 1Gyr) planet and its host star are 1000–2000 K and 6000 K, respectively, the thermal light flux ratio is about 10^{-4}–10^{-6} at near-IR wavelengths. Thus, the brightness of the planet and star differ by $\Delta m \sim$ 10–15 magnitudes. For instance, according to the evolutionary model, the estimated H magnitude of a 100-Myr-old planet with mass 10 $M_{\rm J}$ located 100 pc away is $\sim$ 19 mag (Baraffe et al. 2003).

Wavefronts of light emitted by star/planet systems are disturbed by turbulence in the atmosphere and telescopic aberrations. To improve the star image, perturbed wavefronts are corrected by adaptive optics (AO), which contains a deformable mirror and other apparatus. AO improves the Strehl ratio, the ratio of the peaks of the point spread function (PSF) obtained by perfect and real optics. By increasing the signal-to-noise ratio (S/N) of the planet, smaller planets can be detected. Coronagraphy blocks the light from bright sources (stars) to reveal surrounding faint sources (planets and other low-luminosity objects). This filtering improves contrast between the planet and its host star. Nonetheless, planetary detection is limited by residual noise, including quasi-static noise, after AO processing. A high-contrast imaging technique can be realized by differential imaging, which reduces these noises by subtracting the reference image from all images. In some methods, the reference image is constructed by image rotation

(notably, angular differential imaging: ADI), difference wavelength (spectral differential imaging: SDI), polarization (polarization difference imaging: PDI) and others. ADI will be discussed in Section 2.2.

1.2 Planet formation and their orbital evolution

Understanding planet-building and its evolutionary process is among the most challenging problems in astrophysics. The main competing theories for gas-giant planets formation are core accretion (*e.g.*, Mizuno 1980; Pollack et al. 1996) and disk instability (*e.g.*, Cameron 1978; Kuiper 1951). Planet formation theories have been continuously updated or newly proposed (*e.g.*, Inutsuka et al. 2010), but these two hypotheses have been retained in most studies.

In the core accretion model, planetesimals grow to planetary cores that subsequently accrete disk gas. In this model, relatively small giant planets such as Jupiter and Saturn are thought to form at distances 10 AU or less from a solar-type host star within several Myr (Ida & Lin 2004; Pollack et al. 1996). This model explains why more gas-giant planets surround stars with higher metallicity(Fischer & Valenti 2005; Matsuo et al. 2007) and also explains the formation of rocky planets such as the Earth.

In the disk instability model, a cold and dense region of the gaseous disk becomes gravitationally unstable, and collapses into fragments that eventually form gas-giant planets. In this model, planets of a few to 10 $M_{\rm J}$ can be created within a few 10–100 AUs from the central star on a dynamic timescale of several thousand years (Janson et al. 2012; Kratter et al. 2010; Marois et al. 2008; Rafikov 2007, 2011). These formation models therefore predict two populations of giant planets segregated by orbital distance, with the closer and more distant planets formed by core accretion and disk instability, respectively.

However, planets may subsequently migrate inwards via interaction with the parent disk, or outward in the case of type III migration (Masset & Papaloizou 2003). Furthermore, in a multiple-planet system, a planet can be ejected beyond the outer radius of the disk via gravitational interaction between formed or embryonic planets (*e.g.*, Basu & Vorobyov 2012; Ida & Lin 2004; Veras et al. 2009). In addition, free-floating planets may be captured at wide orbits, although such widely separated planets are likely rare (of the order of a few percent, *e.g.*, Kouwenhoven et al. 2010). Thus, the formation and evolution of planets has been

theoretically explored, and a number of plausible mechanisms proposed, but experimental observations of planet frequency over a wide range of orbital distances are important to verify or refute these theories.

1.3 Planet frequency

Determining planet frequency is another important and interesting problem. In 1967, Frank Donald Drake estimated the number of extraterrestrial civilizations N currently existing in the Galaxy as

$$N = N_S \cdot f_P \cdot ne \cdot fl \cdot fi \cdot fc \cdot fL. \tag{1.6}$$

In Equation 1.6 (later revised by Sagan 1983), f_P is the fraction of stars with planetary systems (Maccone 2012, p.8)[2]. In addition, to explore the planet formation and evolution theories, the fractions of planets occupying different regions of the mass versus semi-major axis must be evaluated.

To date, over 1000 extrasolar planets have been found by observation, of which approximately 90% were detected by radial velocity (RV) and transit observations (*e.g.*, Fressin et al. 2013; Howard et al. 2012; Mayor et al. 2011). This rapidly growing sample allows a statistical discussion of planet frequency based on the properties of the planets and their host stars. Hot Jupiters ($P < 10$ days) are considered to be rare ($< 1.5\%$; Cumming et al. 2008; Howard et al. 2012; Wright et al. 2012). However, these observing methods have a limitation: it is difficult to detect planets that are far from their host stars, i.e., more than about 10 AU. Direct imaging, which is sensitive to such distant regions, can provide critical and complementary information to that obtained by indirect detection methods (Carson et al. 2013a; Currie et al. 2011; Lagrange et al. 2010; Marois et al. 2008, 2010). Given its importance and the development of instruments and observing techniques, direct imaging has been extensively performed in recent years with large-aperture telescopes. Based on Gemini observations of 85 stars, Lafrenière et al. (2007) calculated the frequency of planets around single stars as less than 10% (for separations in the range 50–250 AU and planet masses 0.5–13 $M_{\rm J}$). In Nielsen

[2] N_S, denotes the number of stars in the Milky Way Galaxy;
ne, the number of planets in a given system that are ecologically suitable for life;
fl, the fraction of otherwise suitable planets on which life actually arises;
fi, the fraction of inhabited planets on which an intelligent form of life evolves;
fc, the fraction of planets inhabited by intelligent beings who develop a communicative technical civilization; and
fL, the fraction of planetary lifetime graced by a technical civilization.

& Close (2010), estimated that less than 0.2% of single stars were surrounded by planets (8.9–911 AU, $> 4\ M_{\rm J}$). This figure was obtained by compiling data of 118 stars (Biller et al. 2007; Lafrenière et al. 2007; Liu 2004; Marois et al. 2006; Masciadri et al. 2005). Moreover, Chauvin et al. (2010) analyzed VLT observations of 88 targets (10–500 AU, $> 1\ M_{\rm J}$) and obtained a frequency below 10%. Vigan et al. (2012) reported the frequency of planets around early type stars (A–F) as $8.7^{+10.1}_{-2.8}$ (1σ). The frequencies of stars hosting planets, obtained by direct imaging surveys, are summarized in Table 1.1. The problem with direct imaging is the much smaller sample size than is available from indirect observation.

In these imaging studies, the targets belong to moving groups and local associations such as the β Pictoris moving group, TW Hya Association, Tucana–Horologium Association, and AB Doradus group (Chauvin et al. 2010; Lafrenière et al. 2007). Because these associations are nearby (20–100 pc) and young (several to several hundred Myr), their planets are relatively bright and should be easily detectable. In addition, stars in the same cluster are similarly aged and approximately the same distance from Earth. This similarity statistically improves the accuracy of the age and luminosity estimates and, in turn, the derived planetary mass. However, the number of group members is relatively small. Such sparse moving groups contain only several dozen members each, and only a dozen stars have been observed in previous studies (Chauvin et al. 2010). In contrast, open clusters usually contain many more members, a factor that assists in determining the frequency of planets at specific ages and accurately estimating planetary masses.

For this reason, we have started an imaging survey of planets in an open cluster, Pleiades, in which the frequency of gas-giant planets is constrained beyond >50 AU of the member stars. Imaging is performed using the near-infrared instrument HiCIAO installed with AO188 adaptive optics on the Subaru telescope (Hodapp et al. 2008; Suzuki et al. 2010). Here we report the imaging results of 20 stars surveyed in the Pleiades cluster.

TABLE 1.1: Summary of previous planet frequency observations.

Author	Sp. Type (median)	Target cluster [1]	Age (Myr) (median)	Distance (pc) (median)	Number	Investigated range Mass (M_J)	Separation[2] (AU)	Planet frequency (%)
Direct imaging								
Lafrenière et al. (2007)	F2–M4 (K0)	1, 2, 3, 5, 8, 9, 10, 11, 14	10–300 (100)	3.2–34.9 (22)	85	0.5–13	50–250 (sma)	$\leq$9.3
Chauvin et al. (2010)	B7–M8	2, 3, 4, 5, 6, 7, 12, 14	8–100 (30)	10–130 (42)	88	0.5–15	10–500 (pro)	< 10
Heinze et al. (2010)	F0–M6 (K2)	-	100–5000 (300)	3.27–43.3 (11.2)	54	5 10	30–94 22–100	< 50 < 15
Nielsen & Close (2010)	A5–M5 (K1)	1, 2, 3, 5, 8, 9, 10, 11, 12, 12, 13, 14	2–8800 (160)	3.2–77.0 (24)	118	> 4	8.9–911 (sma)	< 20
Vigan et al. (2012)	A0–F5 (A3)	-	8–400 (100)	19–84 (50)	42	3–14	5–320 (sma)	$8.7^{+10.1}_{-2.8}$
Rameau et al. (2013)	B–M (F)	2, 3, 8, 12	5–300 (50)	3.29–150 (50.58)	59	1-13	1–1000 (sma)	$22.0^{+37.4}_{-15.3}$
Frequency of brown dwarf mass companion by direct imaging								
Metchev & Hillenbrand (2009)	F5-K5 (G5)	1, 15, 16, 17 the Pleiades	3–500 (200)	10–190 (46)	266	12–72	28–1590 (sma)	$3.2^{+3.1}_{-2.7}$
Leconte et al. (2010)	A0–K5 (G0)	-	100–11000 (2400)	3.48–49 (17.5)	58	> 40	10–50	< 20
Lodieu et al. (2012a)	BD[3]	the Pleiades	125 ± 8	120	51+137 (systems)	30–75	<100–200 (pro)	$24.3^{+7.4}_{-7.3}$
Microlensing								
Cassan et al. (2012)	-	-	-	-	-	0.3–10	0.5–10 (pro)	17^{+6}_{-9}
Radial velocity								
Cumming et al. (2008)	F–M	-	-	-	585	0.3–10	0.03–3.1 (sma)	10.5
Mayor et al. (2011)	F–K	-	-	-	822	> 0.3	< 5 (sma)	14
Bonfils et al. (2013)	M0–M6 (M3)	-	-	-	102	< 3	< 1 (sma)	1–5
Transit								
Howard et al. (2012)	-	-	-	-	-	Giant ($8R_\oplus$–$34R_\oplus$)	< 50days	1.3 ± 0.2
Fressin et al. (2013)	M G-K F	-	-	-	-	Giant ($6R_\oplus$–$22R_\oplus$)	< 1.06 (sma)	3.6 ± 1.7 6.1 ± 0.9 4.3 ± 1.0

[1] Moving groups: (1) α Persei; (2) AB Doradus; (3) β Picoris; (4) Carina; (5) Carina-Near; (6) Columba; (7) η Cha; (8) Hercules-Lyra; (9) IC2391; (10) Local association; (11) Local association subgroup B4; (12) Tucana-Horologium; (13) TW Hydrae association; (14) Ursa Major; (15) Sco-Cen; (16) Upper-Sco; (17) Hyades.

[2] Separation: sma: semi-major axis; pro: projected separation [3] $K1 \sim 14.32$–16.27 mag.

Chapter 2

Observation

2.1 Target selection

2.1.1 Selection of open clusters

In selecting the open clusters, the sensitivity for detecting gas-giant planets of $<$10 $M_{\rm J}$. The luminosity of a planet depends on its age and mass.

The formation process itself may also be related to the luminosity evolution of the planet. Two types of planetary luminosity evolutionary models have been proposed; *hot-start* and *cold-start*. Since the hot-start model assumes higher entropy of giant planets, it may correspond to planet formation by the collapse of a gaseous disk (Allard et al. 2000; Baraffe et al. 1998, 2002, 2003; Chabrier & Baraffe 2000), while the cold-start condition may represent core accretion process (Fortney et al. 2005, 2008; Marley et al. 2007). In addition, higher initial entropy causes brightening of a planet (Spiegel & Burrows 2012). Thus, the brightness of a planet at a certain age is upper-limited by the result derived from the hot-start model and lower-limited by the result of the cold-start model. Examples of hot-stars and cold-start models are the models of Baraffe et al. (2003) and Spiegel & Burrows (2012), respectively. The latter model predicts an H magnitude of 22.6 mag for a planet of mass 12 $M_{\rm J}$, below the sensitivity limits of our equipment. Since planet mass estimates depend on the assumed evolutionary model, we should be aware of such uncertainties.

The relationships between planet age and its H magnitude predicted by various evolutionary models are shown in Figure 2.1. Also shown are the apparent H magnitudes transformed from the absolute magnitudes in each of nine nearby open

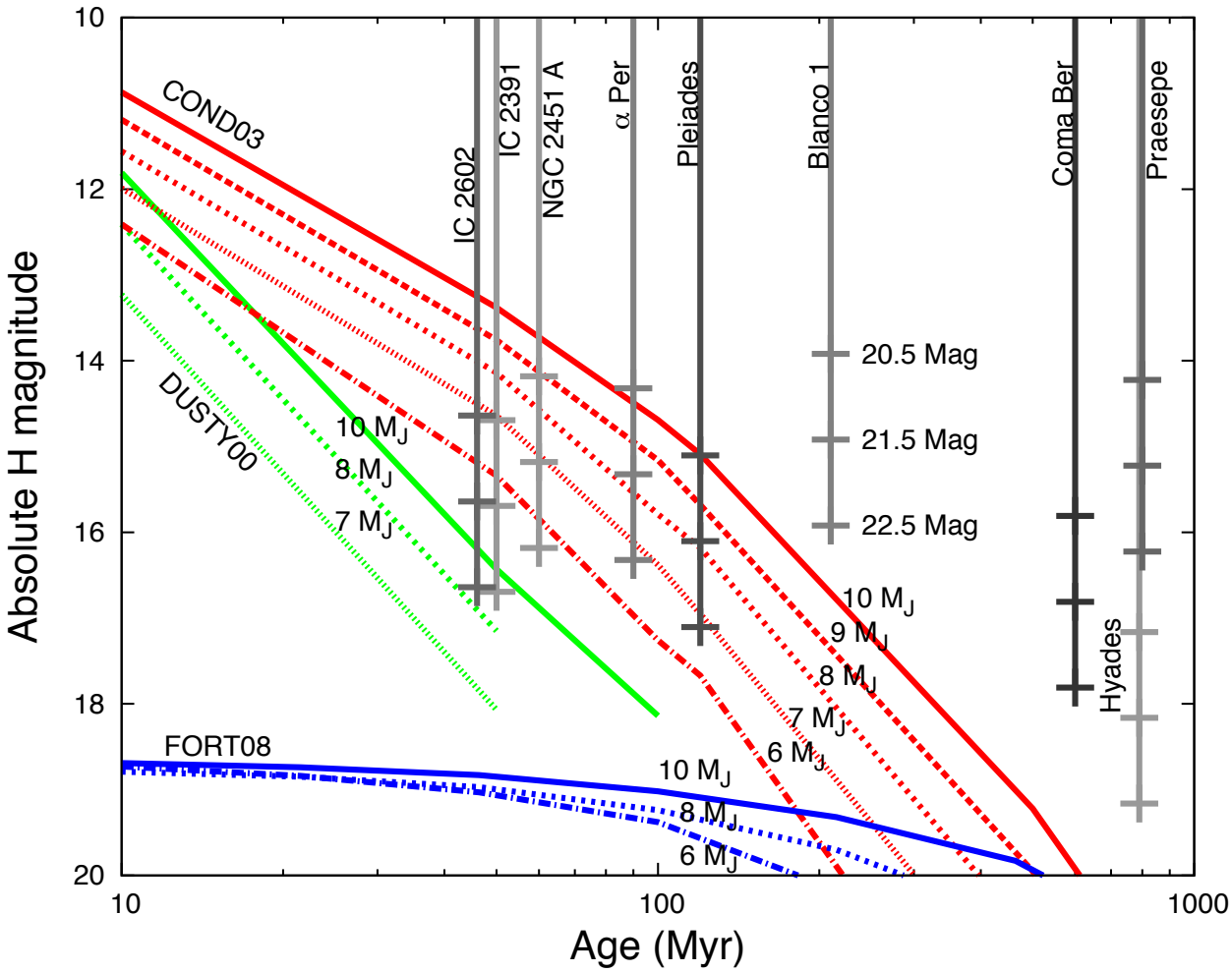

FIGURE 2.1: Absolute H magnitude as a function of age predicted by different evolutionary model. The green, red and blue lines present the result of the DUSTY00 model (Allard et al. 2000; Baraffe et al. 2002; Chabrier & Baraffe 2000), the COND03 model (Baraffe et al. 2003) and the FORT08 model (Fortney et al. 2005, 2008; Marley et al. 2007), respectively. Vertical gray lines present the detectable magnitudes (20.5, 21.5 and 22.5 in the H band) on open clusters, and their ages (see Table 2.1 for details). The apparent magnitude change depends on the distance to the cluster.

clusters. The properties of each cluster are summarized in Table 2.1. Four clusters contained no planet detections fitting any of the evolutional models (Blanco 1, Coma Ber, Hyades, and Praesepe cluster). The members of four of the remaining clusters (IC 2602, IC 2391, NGC 2451 A, and α Per) are smaller than the Pleiades members.

Therefore, we selected the Pleiades, a nearby young star cluster observable from the northern hemisphere. The Pleiades cluster is significantly populous and thus provides a better probe for determining planetary frequency of a given age

TABLE 2.1: Open clusters within 250 pc

Name	Distance[1] (pc)	Age[1] (Myr)	Metallicity[5] [Fe/H]	Member
IC 2602	148.6	46.[2]	$+0.00 \pm 0.01$[6]	> 25[10]
IC 2391	144.9	50.[3]	-0.01 ± 0.02[6]	~ 130[11]
NGC 2451 A	183.5	60.[4]	-0.06[7]	> 70[12]
α Per	172.4	90.[5]	-0.05 ± 0.06	~ 140[13]
Pleiades	120.2	120.	$+0.03 \pm 0.04$[8]	~ 1300[14]
Blanco 1	207.0	210.	$+0.04 \pm 0.02$[9]	~ 380[15]
Coma Ber	86.7	600.	-0.05 ± 0.06	~ 150[16]
Hyades	46.5	790.[4]	$+0.13 \pm 0.06$[4]	~ 200[17]
Praesepe	181.5	800.	$+0.04 \pm 0.06$	~ 1050[16]

[1] van Leeuwen (2009).
[2] Dobbie et al. (2010). [3] Barrado y Navascués et al. (2004). [4] Pöhnl & Paunzen (2010). [5] Lodieu et al. (2012b).
[5] Gratton (2000). [6] D'Orazi & Randich (2009). [7] Netopil & Paunzen (2013).
[8] Soderblom et al. (2009). [9] Ford et al. (2005).
[10] Garcia et al. (1988). [11] Barrado Y Navascues et al. (2001). [12] Balog et al. (2009). [13] Makarov (2006). [14] Lodieu et al. (2012a). [15] Moraux et al. (2007).
[16] Kraus & Hillenbrand (2007). [17] Perryman et al. (1998).

and for a common star-formation history. The Pleiades cluster is located at 133.5 $\pm$1.2 pc from Earth (An et al. 2007; Soderblom et al. 2005) and is 125 $\pm$8 Myr old (Stauffer et al. 1998). van Leeuwen (2009) reported a closer distance of 120.2 ± 1.9 pc. However, the difference in distance modulus between these two results is small ($\sim$ 0.2 mag: 5.66 at 133 pc and 5.49 at 120 pc), and similar to the photometric error. The typical metallicity of the cluster members is similar to that of the Sun; [Fe/H]= $+0.03 \pm 0.04$(Soderblom et al. 2009).

To ensure consistent planet brightness between our results and those of previous studies, we adopted the evolutionary model of COND03 (Baraffe et al. 2003). In this model, the H-band magnitudes of a 125 Myr are estimated as 27.9, 22.5, and 20.4 mag for masses of 1, 5, and 10 $M_{\rm J}$, respectively. The typical integration time in our HiCIAO/AO188 observations is approximately 30 min, as described later, yielding a detection limit (5σ) of 21.5 mag. Hence, we can detect planets less massive than 8 $M_{\rm J}$ indicated in Figure 2.1.

2.1.2 Selection of stars in the Pleiades

The target stars in the Pleiades were selected to satisfy three criteria.

1. The star is brighter than 12 mag in the R band.

AO imaging requires a guide star to measure and correct the atmospheric distortion in optical, thus the star should be bright in the R band to obtain near diffraction-limited performance. The Subaru/AO188 configuration requires the guide star to be located within $30''$ of the target; thus, the target star itself is used as the AO guide star.

2. The membership probability is high.

   Cluster membership of the target star is confirmed by three sub-criteria. First, the membership probability should be higher than 80%, based on the proper motion measurements of Belikov et al. (1998), and the target star should not be classified as a non-member by the alternative proper motion tests of Lodieu et al. (2007). Second, if the star fails the first sub-criterion, its membership probability (Belikov et al. 1998) must exceed 50%. The star must also be classified as a member by the test described in Lodieu et al. (2007). Third, if the star satisfies neither of the above sub-criteria, it should be classified as a Pleiades member by the proper motion and photometry of Stauffer et al. (2007).

3. The star has no binary companion that might gravitationally influence its planet formation.

   The target star should not be identified as a binary in the literature (Bouvier et al. 1997; Lodieu et al. 2007; Raboud & Mermilliod 1998). In addition, there should be no other bright (<15 mag in the H band) object in the field of view (FoV) of $20'' \times 20''$ by 2MASS observation.

Finally, we selected 20 targets out of 455 stars in the Pleiades (Belikov et al. 1998; Micela et al. 1996; Pinfield et al. 2003; Raboud & Mermilliod 1998).

2.2 Observation

The twenty selected target stars were observed between October 2009 and December 2012 (Table 2.2). The imaging observations were carried out as part of the Strategic Explorations of Exoplanets and Disks with Subaru (SEEDS; Tamura 2009) using HiCIAO, a high-contrast instrument installed on the Subaru telescope (Hodapp et al. 2008; Suzuki et al. 2010). HiCIAO is equipped with a 2048×2048 HgCdTe/HAWAII 2 detector array and its pixel scale is 9.5 mas/pixel, yielding a field of view (FoV) of $\sim 20'' \times 20''$. The targets were observed with the H or K_S filter, and coronagraphic masks were not used.

TABLE 2.2: Summary of the Pleiades observations.

Name	Sp. Type	Date	Obs. mode/ Filter	H/K_S[4] (mag)	R (mag)	T_{exp} (sec)	N_{exp}	T_{total} (min)	Ang. $_{FoV}$ (°)
BD +22 574	F8[1]	2009-10-31	ADI / H	8.854	10.02	10	207	34.5	116.9
HD 23912	F3V[1]	2009-10-31	ADI / H	8.097	8.88	10	30	5	4.1
		2010-01-23	ADI / H			10	175	29.2	72.8
		2011-01-27	DI / H			10	30	5	-
V1171 Tau	G8[2]	2009-11-01	ADI / H	9.270	10.58	10	30	5	28.1
		2012-12-31	DI / H			30	15	7.5	-
HII 2462	G2[2]	2009-12-22	ADI / H	9.699	10.87	10	60	10	52.8
HD 23863	A7V[1]	2009-12-23	ADI / H	7.599	7.98	10	93	15.5	46.3
HD 282954	G0[2]	2010-01-24	ADI / H	8.851	9.98	10	223	37.2	90.9
		2012-09-12	DI / H			2.5	36	1.5	-
HD 23514	G0[1]	2010-12-01	ADI / H	8.291	8.96	10	204	34	147.6
HD 23247	F3V[1]	2011-01-27	ADI / H	7.811	8.85	10	83	13.8	79.7
		2011-12-23	ADI / H			10	65	10.8	-
V855 Tau	F8[2]	2011-01-28	ADI / H	8.337	9.37	10	160	26.7	114.8
		2012-01-01	DI / H			10	270	45	-
HD 24132	F2V[1]	2011-01-29	ADI / H	7.930	8.59	10	134	22.3	107.9
HD 23061	F5V[1]	2011-01-30	ADI / H	8.325	9.28	10	149	24.8	103.5
TYC 1800-2144-1	G0V[2]	2011-01-31	ADI / K_S	8.868	10.37	10	58	9.7	72.5
HII 1348	K5[2]	2011-12-23	ADI / H	9.831	11.92	10	141	23.5	90.4
Melotte 22 SSHJ G214	G2[2]	2011-12-23	ADI / H	9.634	11.17	10	180	30	59.1
BD +23 514	G5[2]	2011-12-24	ADI / H	9.528	10.90	5	37	3.1	97.3
Melotte 22 SSHJ G213	G2[2]	2011-12-24	ADI / H	9.543	10.91	5	410	34.2	31.4
Melotte 22 SSHJ G221	G2IV[3]	2011-12-25	ADI / H	9.311	10.76	10	221	36.8	41.9
V1054 Tau	–	2011-12-30	ADI / H	9.921	11.35	10	150	25	105.2
	–	2012-09-12	DI / H			10	20	3.3	-
V1174 Tau	–	2011-12-30	ADI / H	10.197	11.61	10	170	28.3	21.3
	–	2012-09-12	DI / H			10	50	8.3	-
Melotte 22 SSHJ K101	–	2011-12-31	ADI / H	9.959	11.69	10	80	13.3	58.4

DI; direct imaging. ADI; angular differential imaging. T_{exp}; integration time of each exposure. N_{exp}; total number of exposures. T_{total}; total exposure time. Ang. $_{FoV}$; rotation angle of field of view during observation.

[1] Wright et al. (2003)

[2] Skiff (2009)

[3] Belikov et al. (2002)

[4] Hmag; Currie et al. (2011), Rmag; Zacharias et al. (2004)

To obtain the required high contrast for probing the close vicinity of the host star, HiCIAO was combined with AO188 (Hayano et al. 2010). The AO achieved a FWHM of 6–10 pixels (0″.05–0″.10) for a point source. Angular differential imaging (ADI; Marois et al. 2006) was also implemented. The ADI imaging method rotates the FoV over time but fixes the detector plane relative to the pupil plane by an image-rotator. Consequently, this method can effectively reduce quasi-static noise, including star halos and speckles produced by the telescope, because the noise pattern is fixed on the detector. Effective noise reduction requires a large field rotation; therefore, the period of the target stars over the meridian was covered by imaging, giving a rotation angle of 25°–150°. In addition, the target star was placed in the center of the FoV to provide a wide area for planet searching.

Our observational procedure proceeded in three steps. First, 5–10 unsaturated frames were taken as a reference for the PSF of the central star. To prevent saturation, the exposure time was 1.5 to 2.5 s. Second, the ADI observations were performed on individual frames over an integration time of 5 or 10 s to obtain high sensitivity, while avoiding smearing caused by the field rotation. The central star was saturated at the peak after this integration time, with a saturated area radius of 3–6 pixels. Third, several unsaturated frames were retaken. Table 2.2 summarizes the information on the observed stars, observing mode, filters, and exposure times of saturated images.

Any sources detected around a target star were considered as planetary candidate companions (CCs). For HD 23247, a bright ($H < 14.5$) companion candidate was detected at 3″.7 from the central star. However, we do not focus on the stellar regime; we are interested in CCs fainter than 14.5 mag, corresponding to masses of approximately 100 $M_{\rm J}$ (brown dwarf mass). CC positions relative to the target star were measured in follow-up observations to determine whether they were co-moving. In the follow-up observations, direct imaging (DI) mode without field rotation was employed since the CCs have wide angular separations (exceeding 3 arcsec). In addition, V1171 Tau, BD+22 574, and HD 282954 were observed with a different camera, Subaru/CIAO, in 2005, which detected the same CCs were detected (Itoh et al. 2011). Thus, we could measure the proper motions by combining our HiCIAO observations with the CIAO results. HD 23912 was observed three times (in October 2009, January 2010, and January 2011) by HiCIAO. Since the field rotation by ADI was too small ($\sim 10°$) for the first imaging in October 2009, it was revisited in January 2010.

Chapter 3

Companion candidates in the Pleiades

3.1 Data reduction

The first step of the image processing was to remove the striped pattern caused by fluctuating bias levels in the individual raw images. The stripes consist of two components: 32 horizontal stripes each with a height of 64 pixels, and thin vertical stripes each 2048 pixels high, randomly distributed over the image. These patterns vary with time and are independent among images. We created the striped pattern for the whole FoV from the sky region in each frame, and subtracted it from the raw frame, a process known as sky subtraction. Next, bad pixels and their clusters were corrected by subtracting the de-striped dark image. We then performed flat-fielding using dome flats. Bad pixels randomly occurring in arbitrary pixel positions were interpolated from the surrounding pixels. These calibrations were conducted using our own reduction tool for HiCIAO data.

The image processing described below was performed with IRAF[1]. Sub-pixel shifts are inevitably introduced during distortion correction and ADI reductions, since pixel values are smeared interpolation of adjacent pixels. Such shifting reduces the noise level in the image. Moreover, the amount of sub-pixel shift differed from frame to frame, and we confirmed that the degree of noise reduction can vary among multiple images. Such a non-uniform process, as well as artificial noise reduction, may affect our discussion of detection limits. Thus, before correcting for distortion, all images were smoothed with a 2-D Gaussian filter with a FWHM of

[1]IRAF is distributed by the National Optical Astronomy Observatories, which are operated by the Association of Universities for Research in Astronomy, Inc., under cooperative agreement with the National Science Foundation.

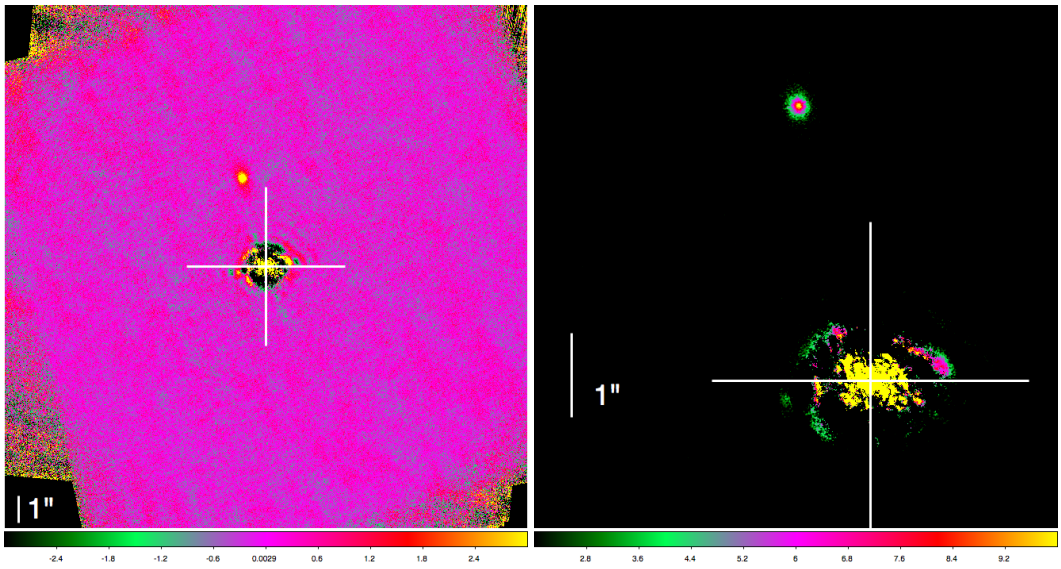

FIGURE 3.1: Image obtained in the H band. The white cross indicates the position of the central star. A point source was detected at an angular separation of 3"38. North and east are directed toward the top and left edges, respectively. *Left panel*: The field of view is $19''.5 \times 19''.5$. The pixel value ranges from -3.0 to +3.0 ADU. The four corners cannot be discussed since these regions are outside the FoV in many frames. *Right panel*: Zoom-in image of the companion candidate. The field of view is $5''.8 \times 5''.8$. The pixel value ranges from +2.0 to +10.0 ADU.

three pixels to obtain the same level of noise reduction for all pixels and images. To measure the distortion, images of the globular clusters M5 and M15 captured by HiCIAO were compared with those of HST/STIS (van der Marel et al. 2002). The distortion was then corrected to obtain a pixel scale of 9.500 ± 0.005 mas/pixel. The precision of the distortion correction is described below.

Next, to prepare the images for ADI reduction, the stellar position was measured and matched to the image center in all frames. The target stars were saturated in areas of radius 3–6 pixels. To remove the stellar halo introduced by ADI reductions, we adopted the centroid position of the halo measured at 10–50 pixels radii as the stellar position. The ADI processing was performed using the standard ADI procedures described by Marois et al. (2006). First, the median of all images was calculated at each pixel position to form a reference image. This reference was then subtracted from each individual frame. The resulting image was de-rotated to align the field so that the top edge indicated north. Finally, the de-rotated images were median-combined with 5σ clipping to ensure sufficient sensitivity for planetary-mass object detection.

An example of a final reduced image is presented in Figure 3.1. This image

was obtained from HD 23912 in the H band data taken in January 2010. The rotation angle of the FoV was 73° and the total integration time was 29.2 min. At the center of the left image, the residual pattern of the subtraction of the stellar halo is visible. A point source is detected at $3''.388 \pm 0''.028$ from the star at a position angle (P.A.) of $14°.92 \pm 0°.48$. If the rotation is slow, additional images are taken at similar P.A. of the field during ADI. The emission from point sources in such images cannot be completely eliminated in the reference image; consequently, self-subtraction occurs in the faint outskirts of the point source. This phenomenon is consistent with sculpting along the azimuthal direction. Images of all target stars are presented in the Section 3.3.

3.1.1 Astrometry

When a CC was detected, its position relative to the central star was measured. The centroid position of the CC was determined by an aperture of radius 1 FWHM. Position was measured in each frame, or frames were combined, depending on the brightness of the CC. To locate the central star in saturated images, we first processed unsaturated images as follows: we determined the offset between the center derived by Gaussian fitting and that derived from a centroiding algorithm with a mask size equal to the saturated area in saturated images. Assuming that the same offset occurs in the saturated images, we corrected the images by this measurement derived by the masked centroiding algorithm. To measure the uncertainty in the position, we verified the deviation from the circular orbit that should result from the FoV rotation under ADI. Once the relative positions were measured in each (combined) image, the rotation center was defined as the center of the fitted circular orbit of the CC in multiple rotated images. Moreover, the position of the CC deviated from its fitted circular path generated by the ADI observation by less than 0.7 pixels. The deviation encompasses possible distortions remaining after the distortion correction (since the fitted path is not perfectly circular), but is small relative to any measurable effects. The results of the astrometry measurements are summarized in Table 3.1.

3.1.2 Photometry

The magnitudes of the central stars and the CCs were measured by aperture photometry, with the target star as the flux calibrator in the case of the CCs. Photometry of the central star was performed on the unsaturated frames taken

TABLE 3.1: Astrometry and photometry of companion candidates.

Name	Separation Angle (″)	P.A. (° E of N)	H (mag)	Mass[1] (M_J)	UT Date	Status
V1171 Tau CC1	12.770 ± 0.025	135.50 ± 0.40	18.3 [2]	-	2005-11-17[3]	-
	12.631 ± 0.033	134.75 ± 0.13	17.8 ± 0.1	22	2009-11-01	-
	12.520 ± 0.023	134.64 ± 0.16	17.8 ± 0.3	22	2012-12-31	B
V1171 Tau CC2	12.880 ± 0.027	136.77 ± 0.40	18.3 [2]	-	2005-11-17[3]	-
	12.744 ± 0.020	136.15 ± 0.10	18.5 ± 0.6	19	2009-11-01	-
	12.628 ± 0.031	135.51 ± 0.21	18.5 ± 0.6	19	2012-12-31	B
V1171 Tau CC3	9.075 ± 0.023	125.94 ± 0.22	19.0 ± 0.9	15	2009-11-01	-
	8.938 ± 0.022	125.35 ± 0.23	19.0 ± 0.9	15	2012-12-31	B
HD 23912 CC1	3.388 ± 0.028	14.92 ± 0.48	17.4 ± 0.1	26	2010-01-23	-
	3.436 ± 0.008	14.52 ± 0.28	17.2 ± 0.2	28	2011-01-27	B
BD +22 574 CC1	3.405 ± 0.025	95.70 ± 0.20	-[4]	-	2005-11-17	-
	3.288 ± 0.033	92.57 ± 0.20	19.2 ± 0.2	13	2009-10-31	PB
BD +22 574 CC2	8.440 ± 0.030	51.82 ± 0.10	18.6 [5]	14	2005-11-17	-
	8.501 ± 0.033	50.01 ± 0.10	17.4 ± 0.2	26	2009-10-31	U
HD 282954 CC1	9.006 ± 0.030	103.82 ± 0.50	16.4 [5]	33	2005-11-17	-
	9.031 ± 0.014	103.23 ± 0.18	14.6 ± 0.1	87	2010-01-23	-
	8.943 ± 0.014	103.28 ± 0.20	14.4 ± 0.2	99	2012-09-12	B
HD 23247 CC1	3.858 ± 0.017	267.24 ± 0.17	11.0 ± 0.2	> 100	2011-01-27	-
	3.832 ± 0.020	267.01 ± 0.20	11.1 ± 0.2	> 100	2011-12-24	C
V855 Tau CC1	8.05 ± 0.03	19.46 ± 0.21	17.2 ± 0.4	27	2011-01-28	-
	-	-	-	-	2012-01-01[6]	?
HD23514 CC1	2.64 ± 0.02	228.7 ± 1.0	-	-	2006-12-10[7]	-
	2.64 ± 0.01	227.8 ± 0.3	-	-	2007-10-25[7]	-
	2.62 ± 0.04	227.2 ± 0.5	-	-	2008-11-04[7]	-
	2.642 ± 0.040	227.51 ± 0.04	15.61 ± 0.08	52	2009-11-01[7]	-
	2.644 ± 0.002	227.48 ± 0.05	15.39 ± 0.06	58	2010-10-30[7]	-
	2.646 ± 0.033	227.59 ± 0.72	15.37 ± 0.05	58	2010-12-01	C
HII 1348 CC1	1.09 ± 0.02	347.9 ± 0.7	-	-	1996-09-25 - 10-01[8]	-
	1.097 ± 0.005	346.8 ± 0.2	15.30 ± 0.09	60	2004-10-03[9]	-
	1.12 ± 0.02	346.8 ± 0.6	-	-	2005-11-21[10]	-
	1.12 ± 0.03	346.1 ± 0.9	15.7 ± 0.4	48	2011-12-23	C
V1054 Tau CC1	7.082 ± 0.014	110.22 ± 0.11	18.1 ± 0.4	20	2011-12-30	-
	7.046 ± 0.022	110.13 ± 0.05	18.1 ± 0.4	20	2012-09-12	B
V1054 Tau CC2	7.361 ± 0.028	76.48 ± 0.22	15.97 ± 0.09	44	2011-12-30	-
	7.329 ± 0.021	75.93 ± 0.10	15.97 ± 0.09	44	2012-09-12	B
V1174 Tau CC1	6.473 ± 0.033	63.68 ± 0.28	18.0 ± 0.4	21	2011-12-30	-
	6.458 ± 0.012	63.67 ± 0.12	18.0 ± 0.4	21	2012-09-12	PC
V1174 Tau CC2	9.24 ± 0.03	37.4 ± 0.2	18.5 ± 0.3	17	2011-12-30	-
	9.23 ± 0.02	37.5 ± 0.1	18.5 ± 0.3	17	2012-09-12	PC

Status sign U denotes "undefined" because of uncertainty in the proper motion measurement. B denotes background object. C and PC indicate a co-moving object and probable co-moving object, respectively. PB denotes a likely background object.

[1] When the CC is a companion, the masses are linearly interpolated as described in Baraffe et al. (2003). [2] The individual brightness of CC1 and CC2 could not be measured, because their spatial separated aperture photometry. In addition, the error was difficult to determine because viewing was poor, leading to fluctuating PSF. [3] Subaru/CIAO, Subaru/IRCS (Itoh et al. 2011). [4] The brightness of the CC was obscured by stellar halo. [5] K magnitude. The error could not be estimated because inclement weather perturbed the PSF. [6] No companion candidates were found in the field of view. [7] Keck/NIRC2 (Rodriguez et al. 2012). [8] CFHT/PUEO (Bouvier et al. 1997). [9] Palomar Hale telescope/PHARO (Geißler et al. 2012). [10] Keck/OSIRIS (Geißler et al. 2012)

before and after the ADI observations, as mentioned in Section 2.2. The background level was estimated as the centroid of the histogram of the pixel values in an annulus with inner and outer radii 50 pixels and 70 pixels, respectively. The aperture radius varied from two to 40 pixels, and its magnitude was taken as the converged magnitude at a radius of about 20 pixels, depending on the targets. Assuming that the star is not variable, the obtained magnitude was compared with that of the 2MASS measurement, enabling conversion from ADU to real magnitude. The photometry of the CCs was performed at the aperture size used for the central star. The flux lost by image processing, including the ADI reductions, was $\sim$ 5%. This loss was estimated by embedding an artificial point source at equally-spaced angles and distances ($1''$ intervals) in the raw image and applying the same reduction procedures. The flux loss was independent of the separation beyond $1''$. The photometry result for the CCs was corrected by the flux loss. Finally, the magnitude of the CCs was calculated using the conversion from ADU to the magnitude derived from the central star photometry. To improve S/N, the CC photometry was performed on combined images of 20–40 frames and the results were averaged. The H magnitudes of the CCs are shown in Table 3.1.

3.2 Detection limits of our observations

The detection limit of our observations is S/N = 5. The noise was determined as the standard deviation of the background level in the azimuthal direction measured at the same distance from the target star. The background level was obtained with an aperture size of approximately 2 $\times$ FWHM on the median-combined image after ADI reduction. The standard deviation (S/N = 1) is plotted as a function of angular separation from the central star in Figure 3.2.

Beyond $1''.5$ from the central star, the median detection limit in all ADI observations tends to 21.0 mag at S/N = 3 and 20.5 mag at S/N = 5. Within $\sim 1''.5$, the detection limit is determined by subtracting the residual of the stellar halo. At separations of $0''.5$ and $1''.0$, the detection limit is 17.7 and 19.7 mag,respectively.

The stellar halo can be better suppressed by techniques other than classical ADI reductions, such as locally optimized combination of images (LOCI: Lafrenière et al. 2007). The LOCI algorithm identifies spatial correlations in the stellar halo and speckle noise from reference images. However, our primary focus is the relatively distant region from the star (exceeding $\sim$100 AU) where uncorrelated,

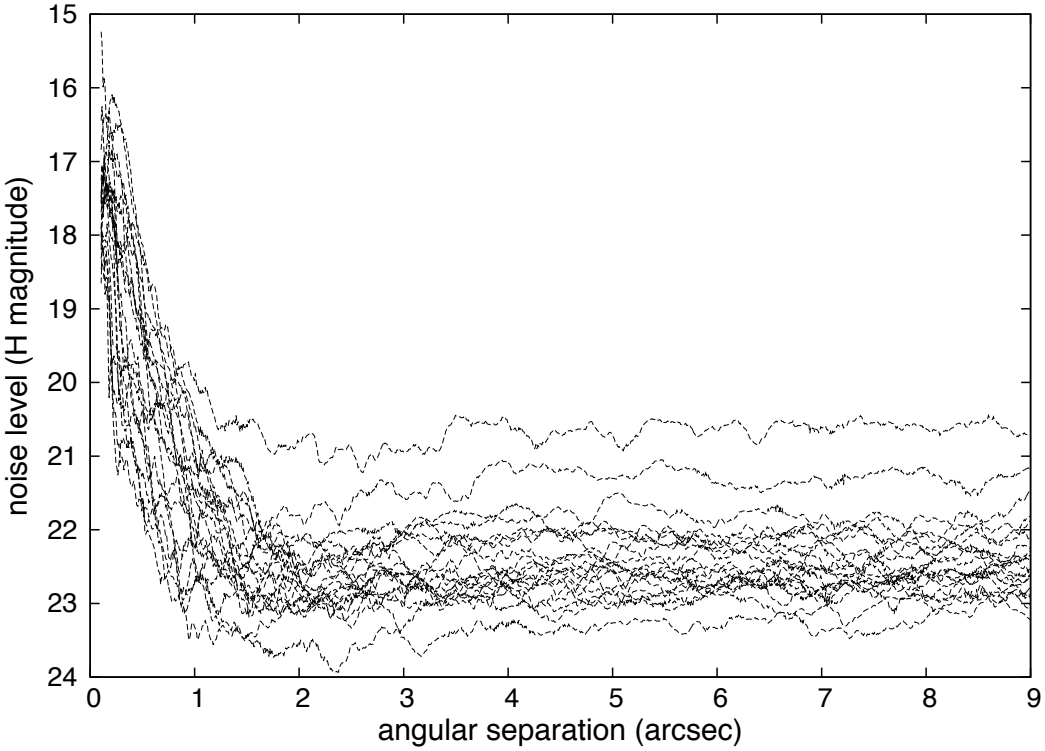

FIGURE 3.2: Noise level (1σ) as a function of angular separation. Dotted lines indicate individual ADI observations obtained from October 2009 to January 2012. The total integration time in each observation ranges from 5–45 min.

random noise dominates. Under these conditions, classical ADI is more effective than LOCI, and is hence adopted in this work.

3.3 Images

All images are shown in Figure 3.3. Details of the images and their reduction are described in Table 2.2 and Section 3.1. All images were obtained by ADI reduction in the H and K_S bands (the exception is Figure 3.3(l); TYC 1800-2144-1). The FoV of all images was $19''.5 \times 19''.5$. The position of the companion candidates (CCs) is indicated by a circle in each image.

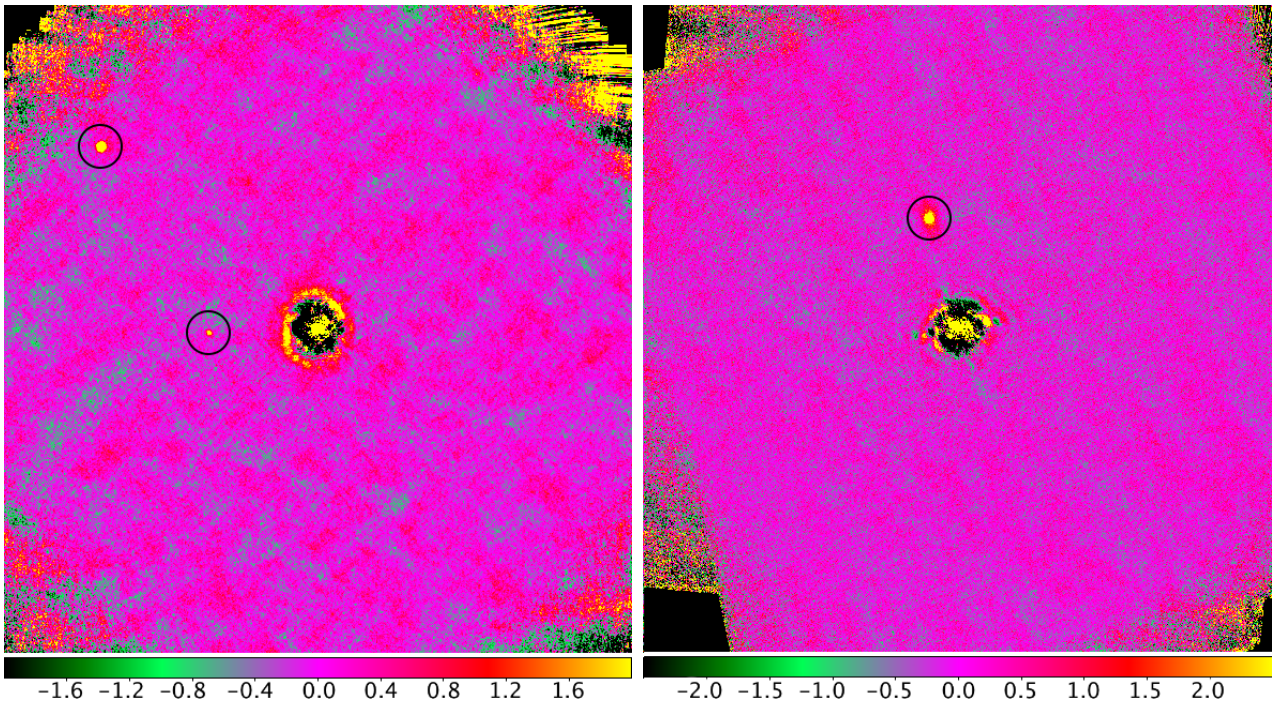

(a) BD+22 574 (Oct. 2009)

(b) HD 23912 (Jan. 2010)

(c) V1171 Tau (Oct. 2009)

(d) HII 2462 (Dec. 2009)

FIGURE 3.3: *Top left panel:* BD+22 574. *Top right panel:* HD 23912. *Lower left panel:* V1171 Tau. The circle in the bottom left corner contains two CCs. *Lower right panel:* HII 2462. The unit of the color bar is ADU per exposure time.

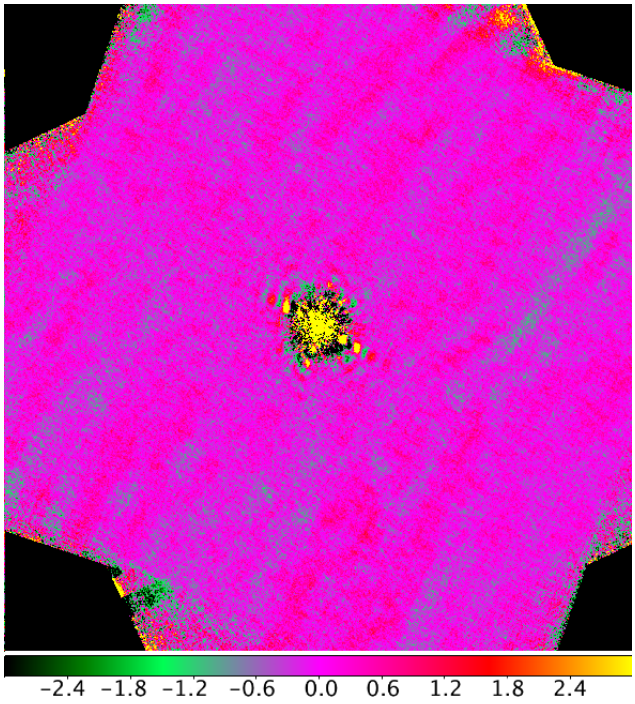

(e) HD 23863 (Dec. 2009)

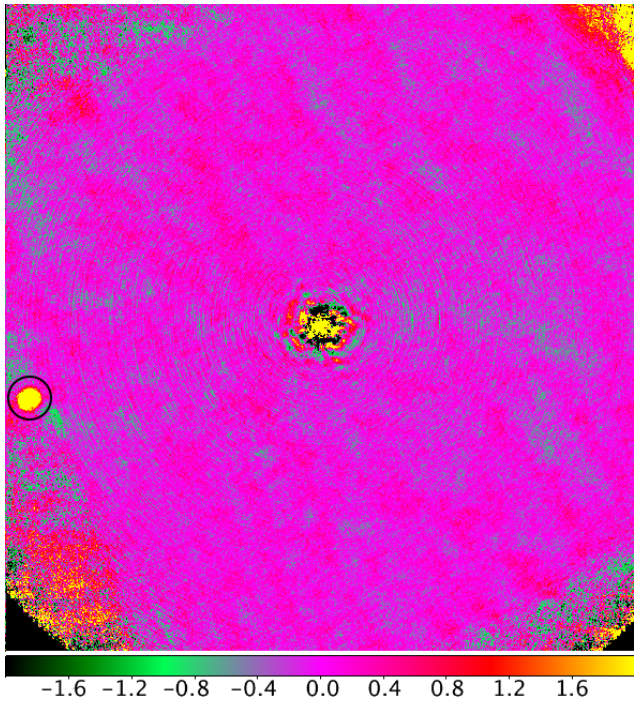

(f) HD 282954 (Jan. 2010)

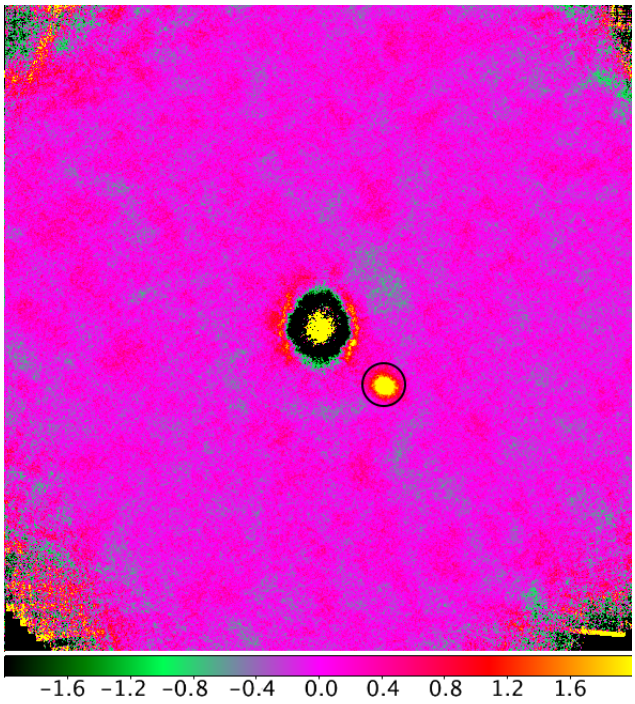

(g) HD 23514 (Dec. 2010)

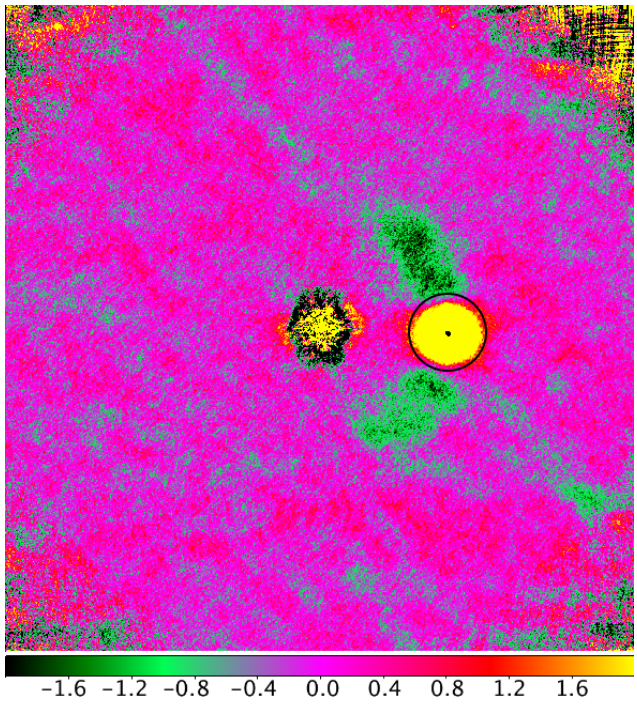

(h) HD 23247 (Jan. 2011)

FIGURE 3.3: *Continued. Top left panel:* HD 23863. *Top right panel:* HD 282954. *Lower left panel:* HD 23514. *Lower right panel:* HD 23247 (2011). The unit of the color bar is ADU per exposure time.

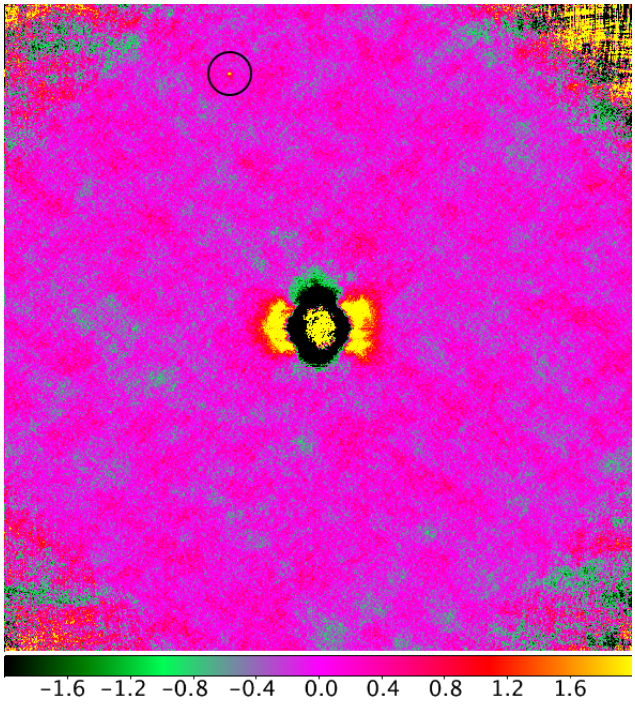

(i) V855 Tau (Jan. 2011)

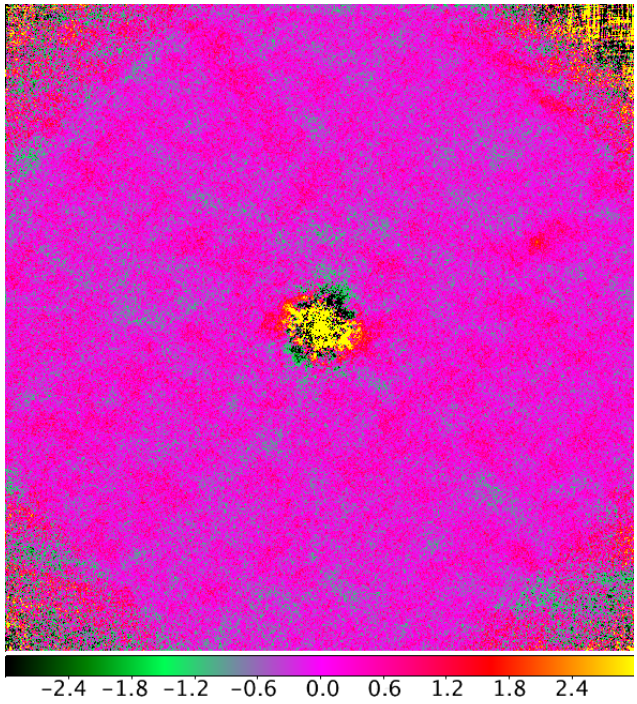

(j) HD 24132 (Jan. 2011)

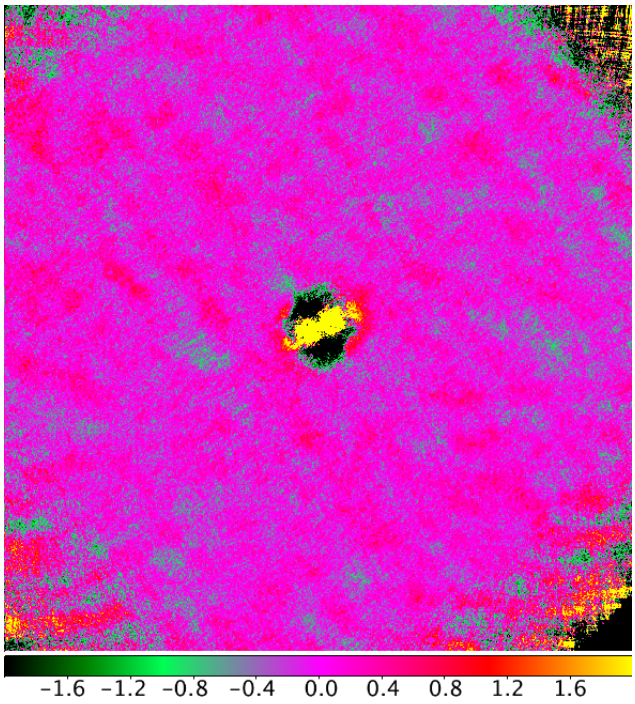

(k) HD 23061 (Jan. 2011)

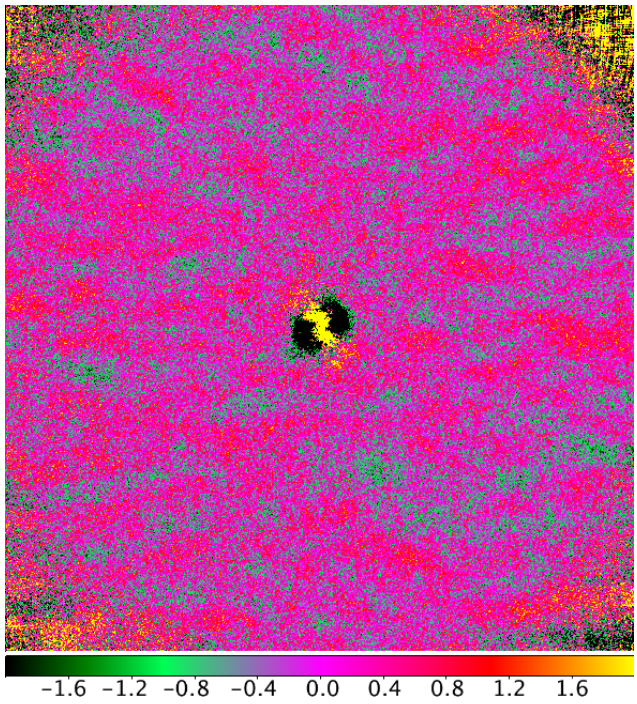

(l) TYC 1800-2144-1 (Jan. 2011)

FIGURE 3.3: *Continued. Top left panel:* V855 Tau (2011). *Top right panel:* HD 24132. *Lower left panel:* HD 23061. *Lower right panel:*TYC 1800-2144-1. The unit of the color bar is ADU per exposure time.

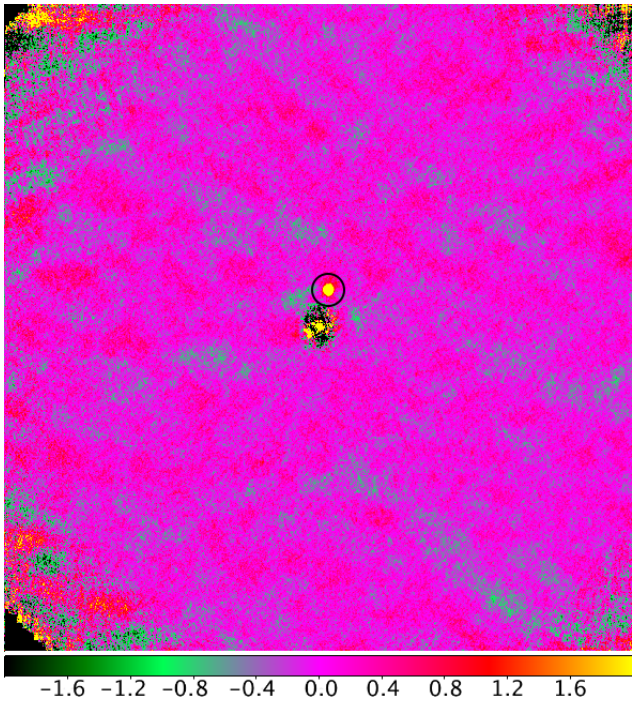

(m) HII 1348 (Dec. 2011)

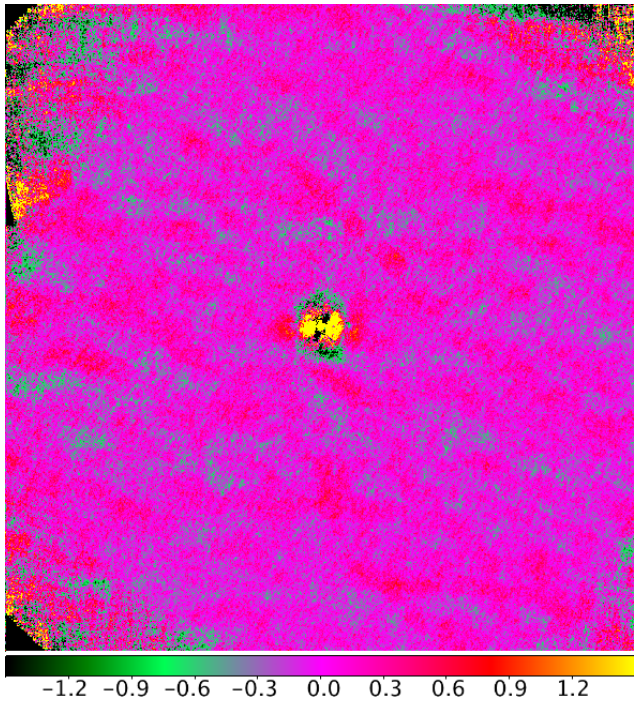

(n) Melotte 22 SSHJ G214 (Dec. 2011)

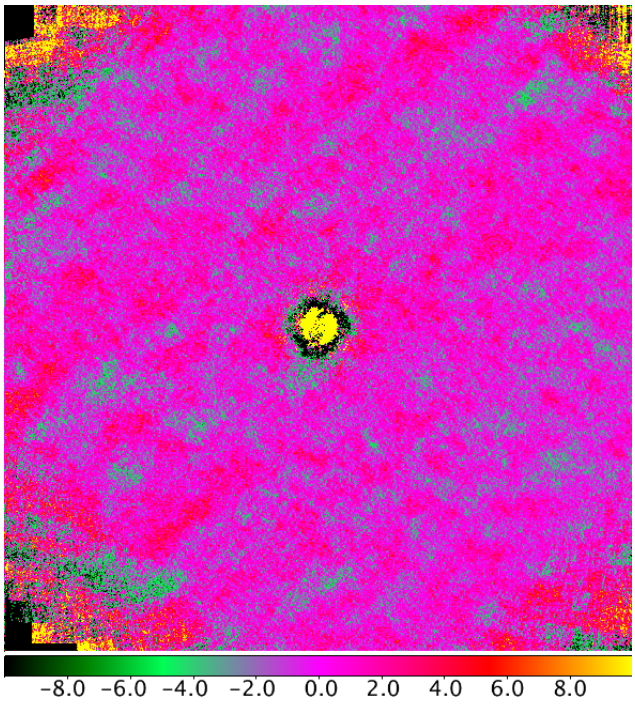

(o) BD+23 514 (Dec. 2011)

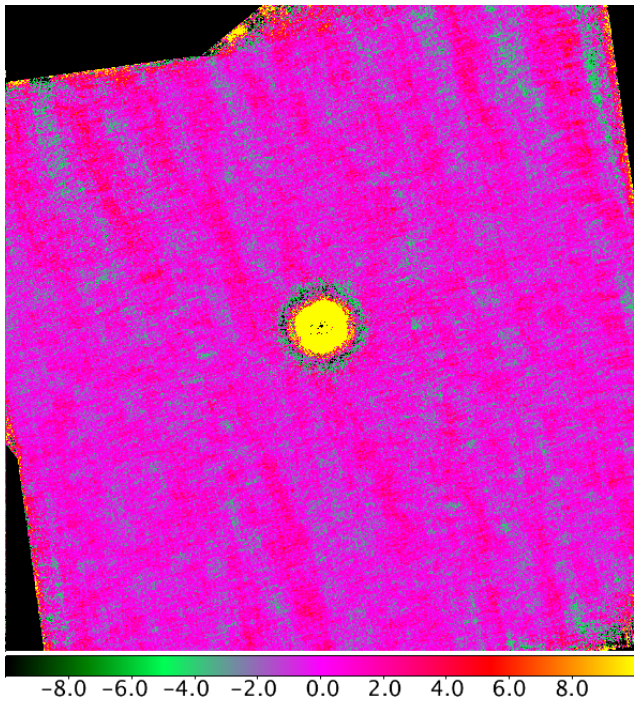

(p) Melotte 22 SSHJ G213 (Dec. 2011)

FIGURE 3.3: *Continued. Top left panel:* HII 1348. *Top right panel:* Melotte 22 SSHJ G214. *Lower left panel:* BD+23 514. *Lower right panel:* Melotte 22 SSHJ G213. The unit of the color bar is ADU per exposure time.

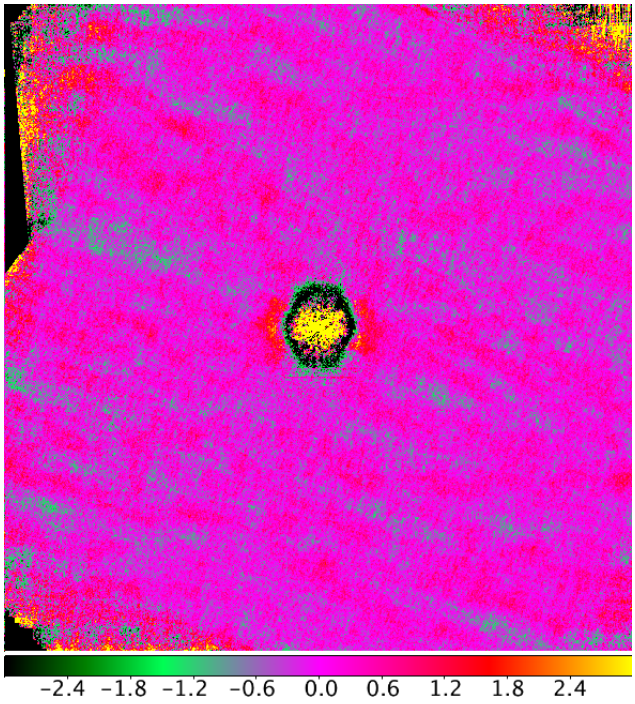

(q) Melotte 22 SSHJ G221 (Dec. 2011)

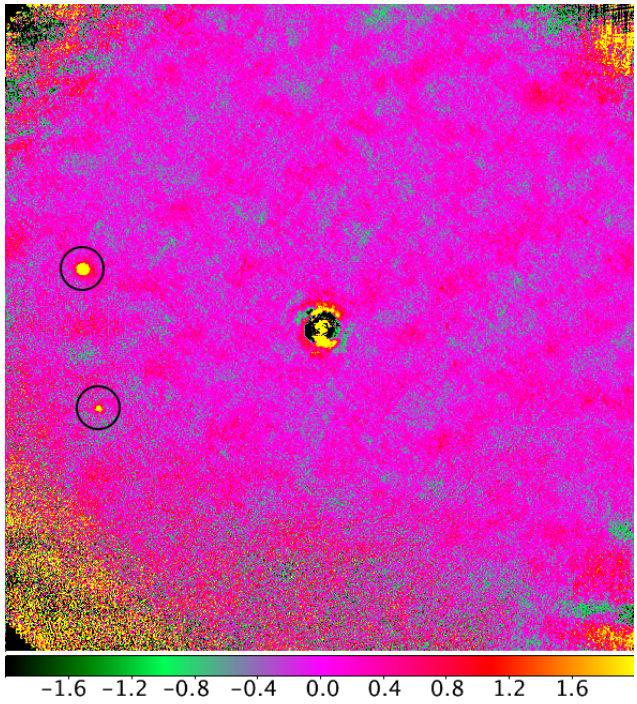

(r) V1054 Tau (Dec. 2011)

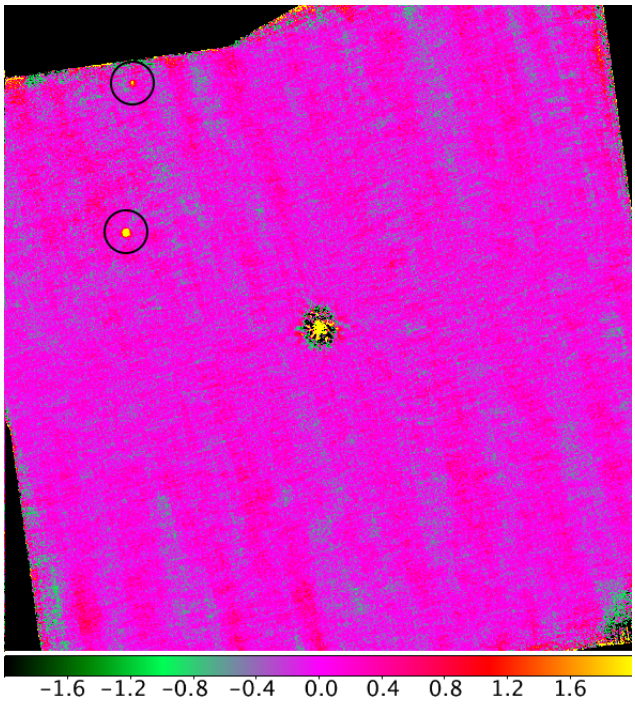

(s) V1174 Tau (Dec. 2011)

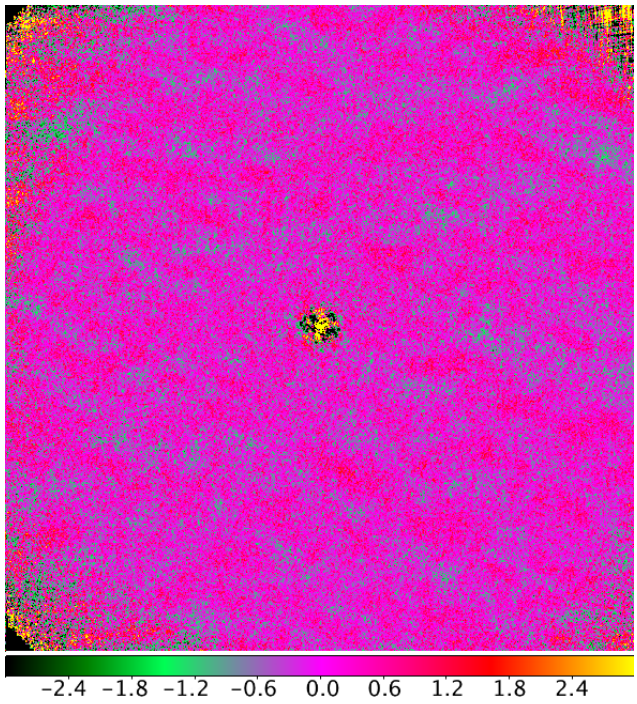

(t) Melotte 22 SSHJ K101 (Dec. 2011)

FIGURE 3.3: *Continued. Top left panel:* Melotte 22 SSHJ G221. *Top right panel:* V1054 Tau. *Lower left panel:* V1174 Tau. *Lower right panel:* Melotte 22 SSHJ K101. The unit of the color bar is ADU per exposure time.

3.4 Astrometry and photometry of companion candidates

Among 15 companion candidates, five CCs for HD 23912, V1054 Tau and V1174 Tau were detected in our follow-up imaging with HiCIAO. The CC of V855 Tau was absent in the follow-up. One CC around HD 23247 proved to be a stellar mass companion. Another eight CCs around five stars (BD+22 574, V1171 Tau, HD 282954, HD 23514, and HII 1348) had been previously observed with Subaru/CIAO, Subaru/IRCS, Keck/NIRC2, CFHT/PUEO, Palomar Hale telescope/PHARO, and Keck/OSIRIS (Bouvier et al. 1997; Geißler et al. 2012; Itoh et al. 2011; Rodriguez et al. 2012). The relative distances of these CCs to their central stars are shown in Figure 3.4.

3.4.1 Confirmed companions in HD 23514, and HII 1348

HD 23514 and HII 1348 are both associated with a co-moving object, most likely a gravitationally-bound companion (Figure 3.4(i) and 3.4(j)). The companion object of HD 23514 was first identified by Rodriguez et al. (2012), while that of HII 1348 was first reported by Geißler et al. (2012). The H magnitudes of the HD 23514 and HII 1348 companions were measured as 15.39 ± 0.06 mag in October 2010 and 15.30 ± 0.09 mag in October 2004, respectively. Their estimated masses are 60 $M_{\rm J}$, placing them in the brown dwarf regime.

Rodriguez et al. (2012) measured the separation and the P.A. of HD 23514 as $2''.642 \pm 0''.003$ and $227°.51 \pm 0°.04$, respectively, in November 2009. In October 2010 these parameters had altered to $2''.644 \pm 0''.002$ and $227°.48 \pm 0°.05$, respectively. In our December 2010 observation, the separation of HD 23514 was $2''.646 \pm 0''.033$ and the P.A. was $227°.6 \pm 0°.7$. The H magnitude of this CC in December 2010 was 15.37 ± 0.05. Our measurements are therefore consistent with those of Rodriguez et al. (2012).

Geißler et al. (2012) measured the separation and the P.A. of the HII 1348 companion as $1''.097 \pm 0''.005$ and $346°.8 \pm 0D.2$, respectively, in October 2004. In November 2005, these were $1''.12 \pm 0''.02$ and $346°.8 \pm 0°.6$, respectively. In our December 2011 observation, the separation of the HII 1348 companion was $1''.12 \pm 0''.03$ and its P.A. was $346°.1 \pm 0°.9$. The H magnitude of this CC in December 2011 was 15.7 ± 0.4. Thus, our measurements are also consistent with those of Geißler et al. (2012).

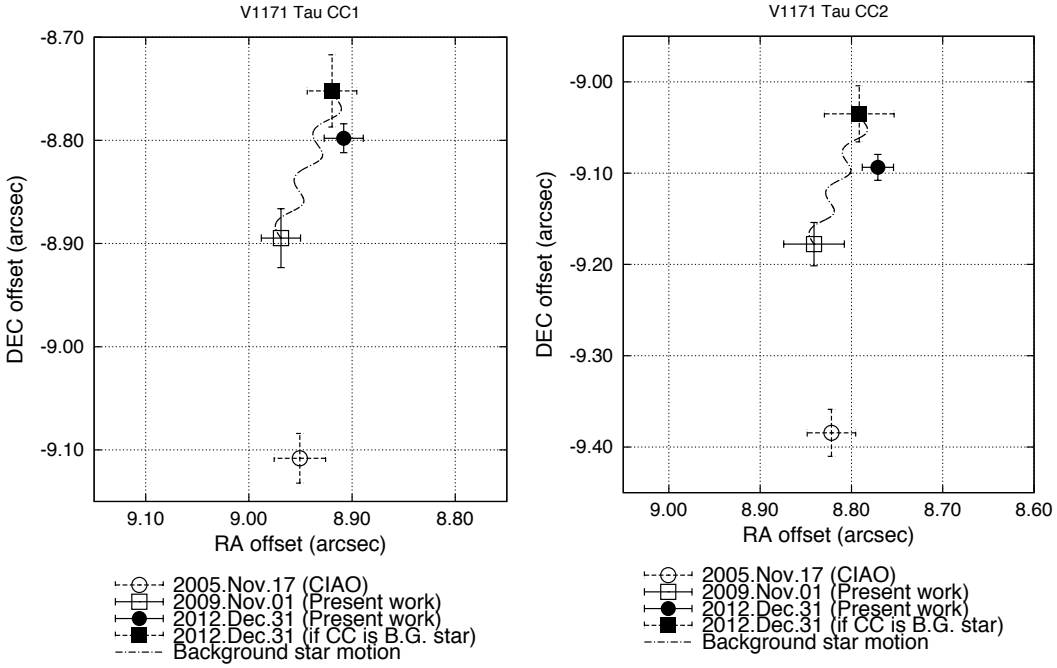

(a) V1171 Tau CC1

(b) V1171 Tau CC2

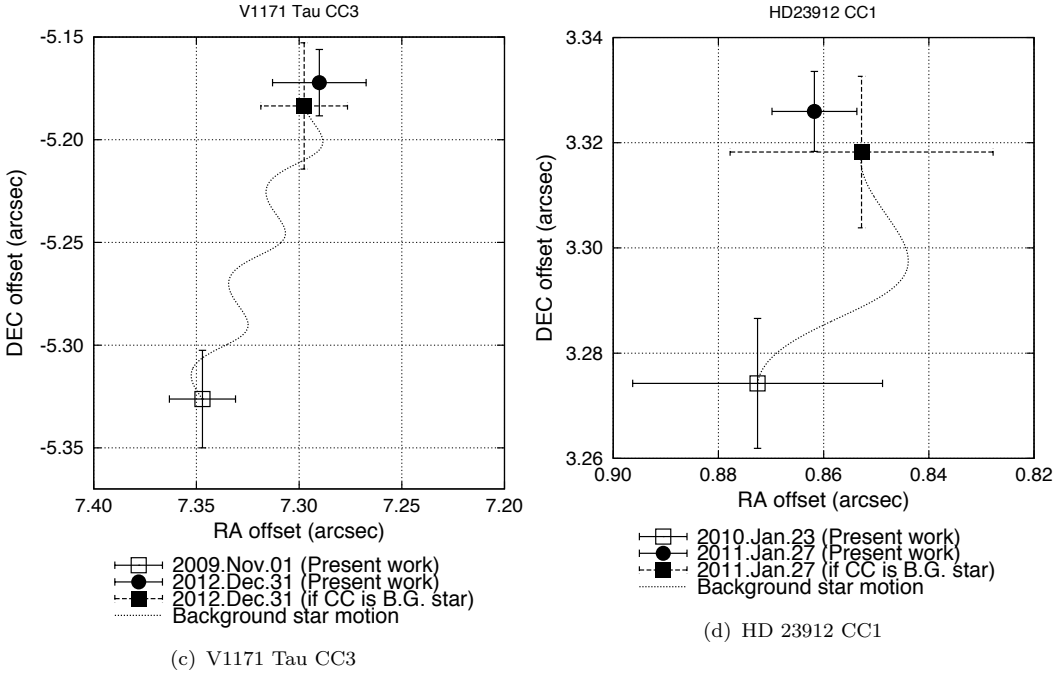

(c) V1171 Tau CC3

(d) HD 23912 CC1

FIGURE 3.4: *Top left panel:* V1171 Tau CC1. *Top right panel:* V1171 Tau CC2. *Lower left panel:* V1171 Tau CC3.*Lower right panel:* HD 23912 CC1.

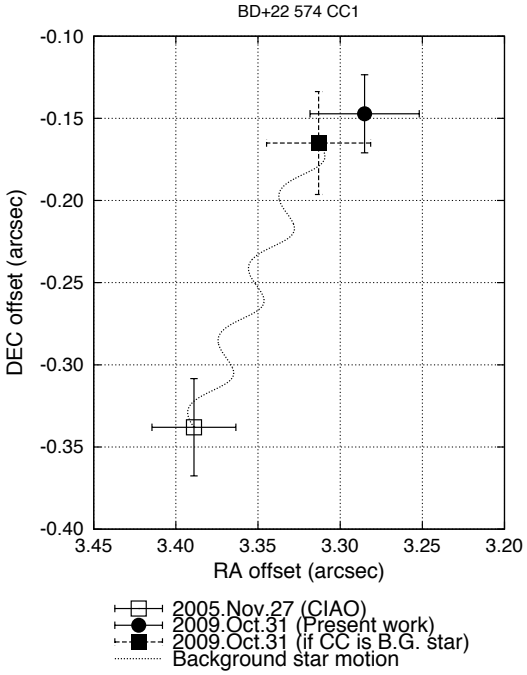

(e) BD+22 574 CC1

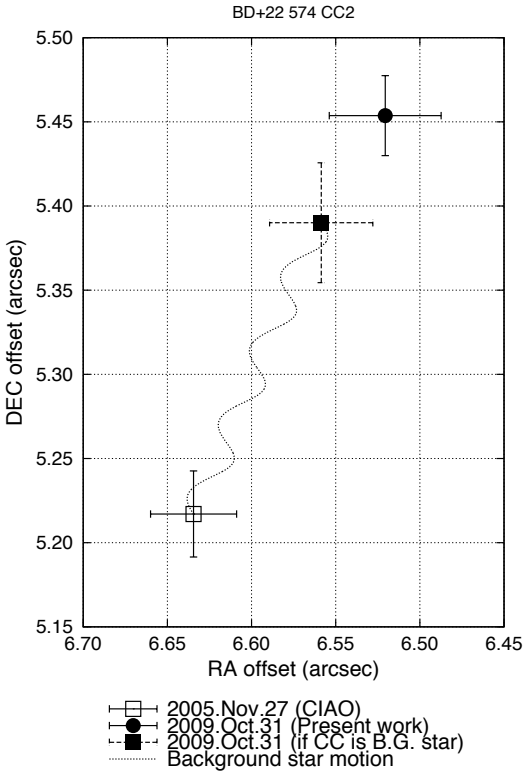

(f) BD+22 574 CC2

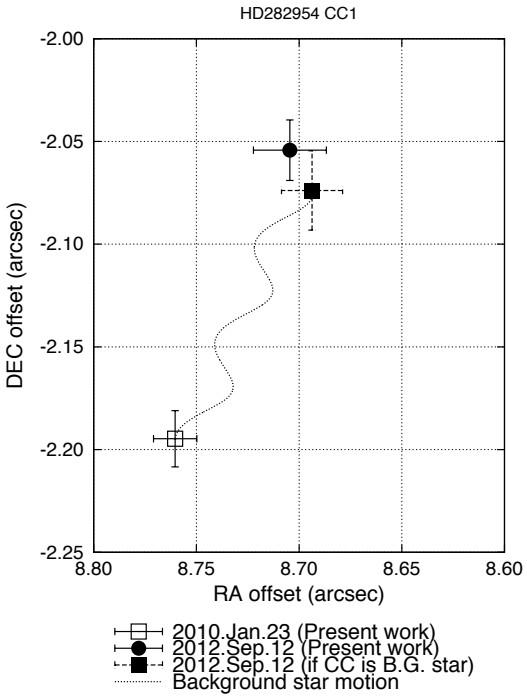

(g) HD 282954 CC1

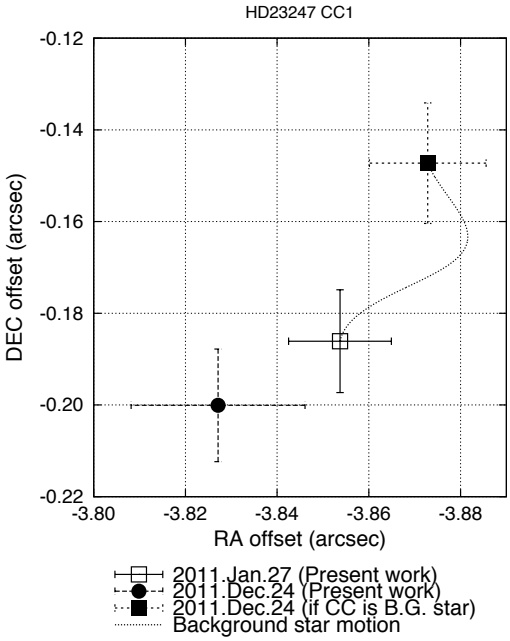

(h) HD 23247 CC1

FIGURE 3.4: *Continued. Top left panel:* BD +22 574 CC1. *Top right panel:* BD +22 574 CC2.*Lower left panel:* HD 282954 CC1.*Lower right panel:* HD 23247 CC1.

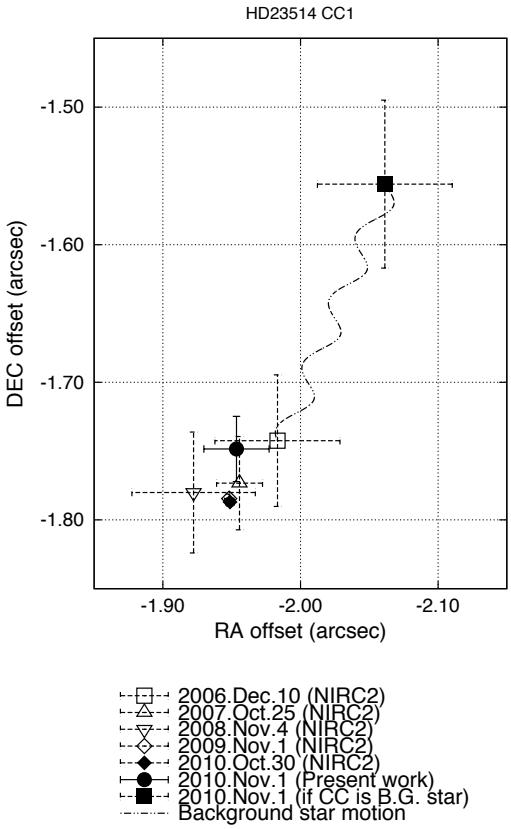

(i) HD 23514 CC1

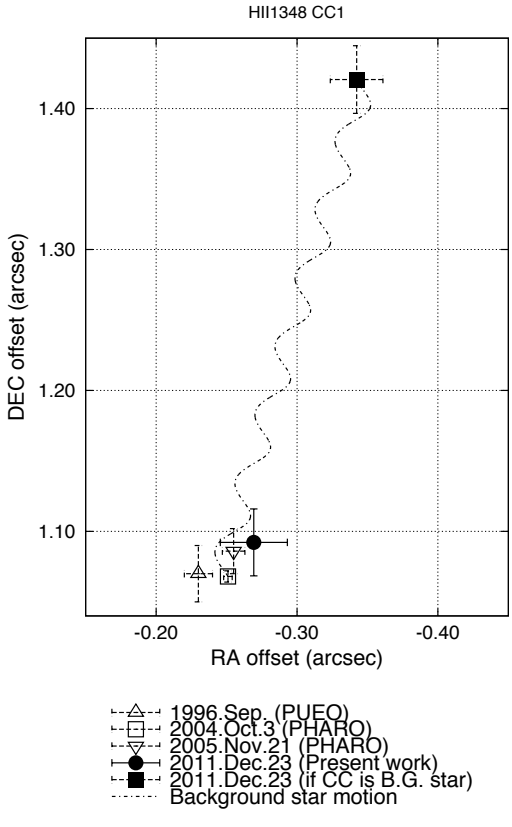

(j) HII 1348 CC1

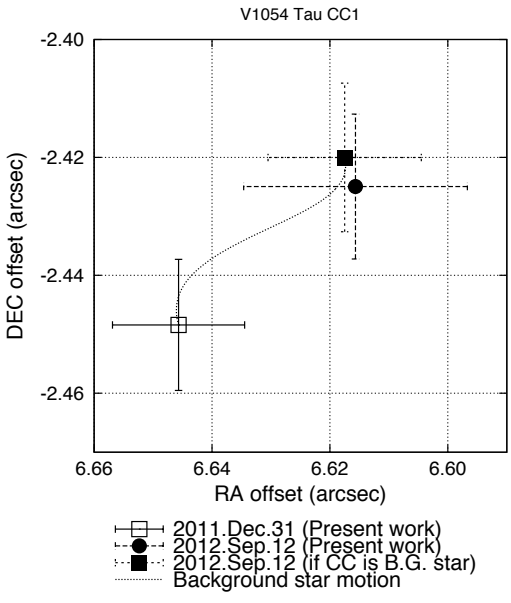

(k) V1054 Tau CC1

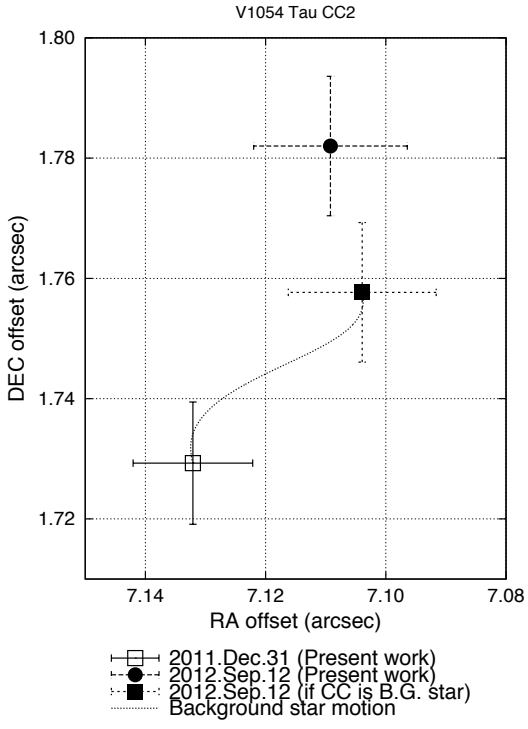

(l) V1054 Tau CC2

FIGURE 3.4: *Continued. Top left panel:* HD23514 CC1.*Top right panel:* HII1348 CC1. *Lower left panel:* V1054 Tau CC1.*Lower right panel:* V1054 Tau CC2.

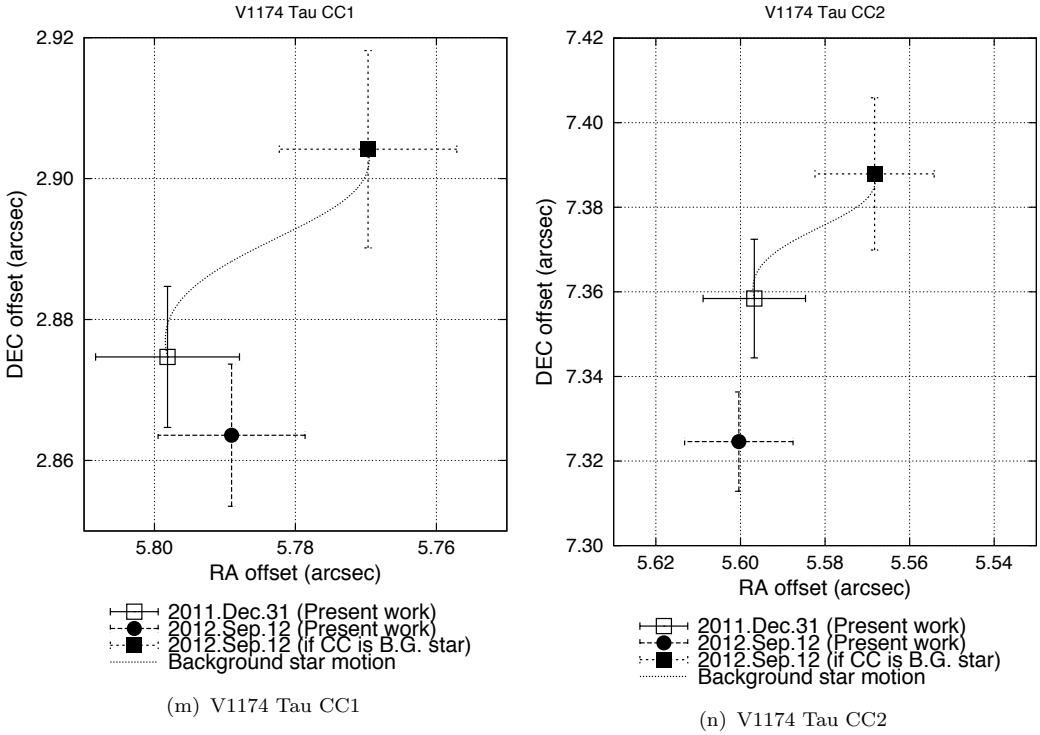

(m) V1174 Tau CC1

(n) V1174 Tau CC2

FIGURE 3.4: *Continued. Left panel:* V1174 Tau CC1. *Right panel:* V1174 Tau CC2.

3.4.2 Background stars on FoV in V1171 Tau, HD 23912, HD 282954 and V1054 Tau

To measure their proper motions with HiCIAO, we made two observations of V1171 Tau, HD 23912, HD 282954 and V1054 Tau. We confirmed that all six CCs were background stars by comparing the astrometry between the two epochs.

3.4.3 BD+22 574

Two CCs of BD+22 574 altered their relative distances to the central star between the two epochs, and are likely to be background stars. The distortion correction is probably imperfect for CIAO data because the distortion map could not be properly generated from the limited number of field stars in Trapezium, the area observed for the distortion correction. However, because the distortion is small at narrow separations, we could confirm that the CC1 of BD+22 574 (separation $\sim 3''.3$) is confirmed as a background star. Whether CC2 of BD+22 574 is also a background star is not clear.

3.4.4 V855 Tau

Although one CC was detected for V855 Tau in January 2011, this candidate was absent in the January 2012 observation. We cannot conclude that the candidate was falsely detected in 2011 because it is not a known artifact, appears in all of the combined images, and the PSF exhibits no unusual shape. Thus, we suggest that this candidate is a foreground object.

3.4.5 The stellar mass companion around HD 23247

A very bright companion candidate was detected within 3″.8 of HD 23247. The H magnitude of this CC was 11.0 ± 0.2 in January 2011, and 11.1 ± 0.2 in December 2011. As evidenced by astrometry (see Figure 3.4(h)), this CC co-moves with HD 23247. Following Baraffe et al. (1998), the estimated mass of this object is 0.5–0.6 $M_{\odot}$ at 120 Myr.

3.4.6 V1174 Tau

V1174 Tau was observed in December 2011 and September 2012. Two CCs were detected and their proper motions were measured by their relative positions to the host star. The separation and P.A. of CC1 was measured as $6''.473 \pm 0''.033$ and $63°.68 \pm 0°.028$ in December 2011, and as $6''.458 \pm 0''.012$ and $63°.67 \pm 0°.12$ in September 2012. The separation and P.A. of CC2 was respectively measured as $9''.24 \pm 0''.03$ and $37°.4 \pm 0°.2$ in December 2011, and as $9''.23 \pm 0''.02$ and $37°.5 \pm 0°.1$ in September 2012. The probability that both objects are co-moving with their host star is high, as shown in Figure 3.4(m)–3.4(n).

V1174 Tau was also observed by the UKIRT Infrared Deep Sky Survey (UKIDSS) in August 2005. CC1 can be detected by the JHK-Band, as shown in Figure 3.5, although CC2 is not visible in this image. Referenced to the star J035035.69+243014.7 (Lawrence et al. 2013), the J, H, and K photometry yields 18.4 ± 0.5, 17.9 ± 0.5, and 18.4 ± 0.5 mag, respectively.

Figure 3.6 is a color-magnitude diagram of V1174 Tau CC1. Although the error in the photometry is large, CC1 of V1174 Tau is similar in color to field L dwarfs (Leggett et al. 2010). If the CC1 is co-moving with V1174 Tau, its likely mass is $17 M_{\rm J}$ based on COND03 (Baraffe et al. 2003). Thus, CC1 presents as the smallest mass companion around a star in the Pleiades cluster.

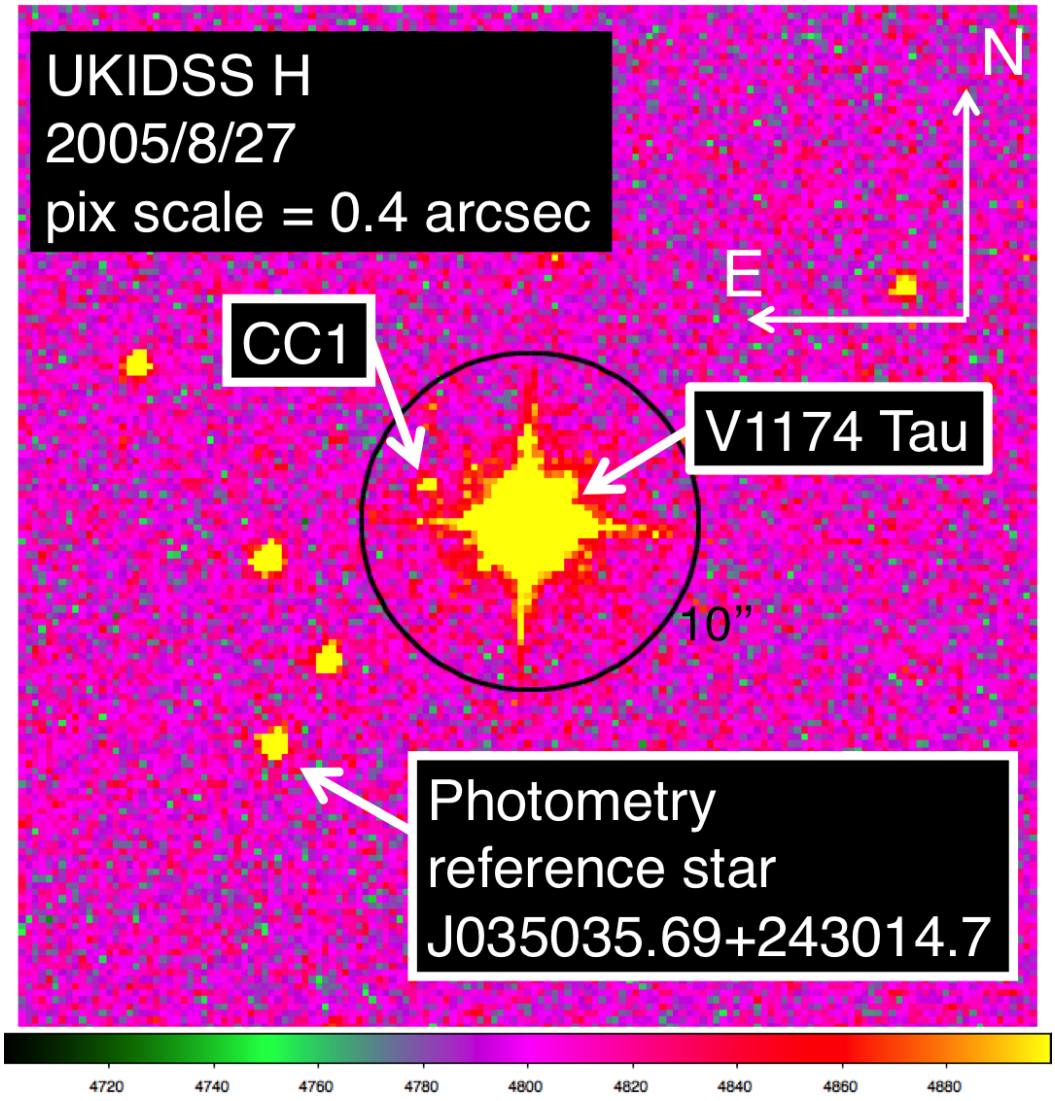

FIGURE 3.5: This image was taken by UKIDSS in October 2005. The central star is V1174 Tau. The black circle delineates a 10 arcsec radius from the central star. CC1 of V1174 Tau and the photometry reference star are also shown. The field of view is $60''.8 \times 60''.8$. The pixel value ranges from +4700 to +4900 ADU.

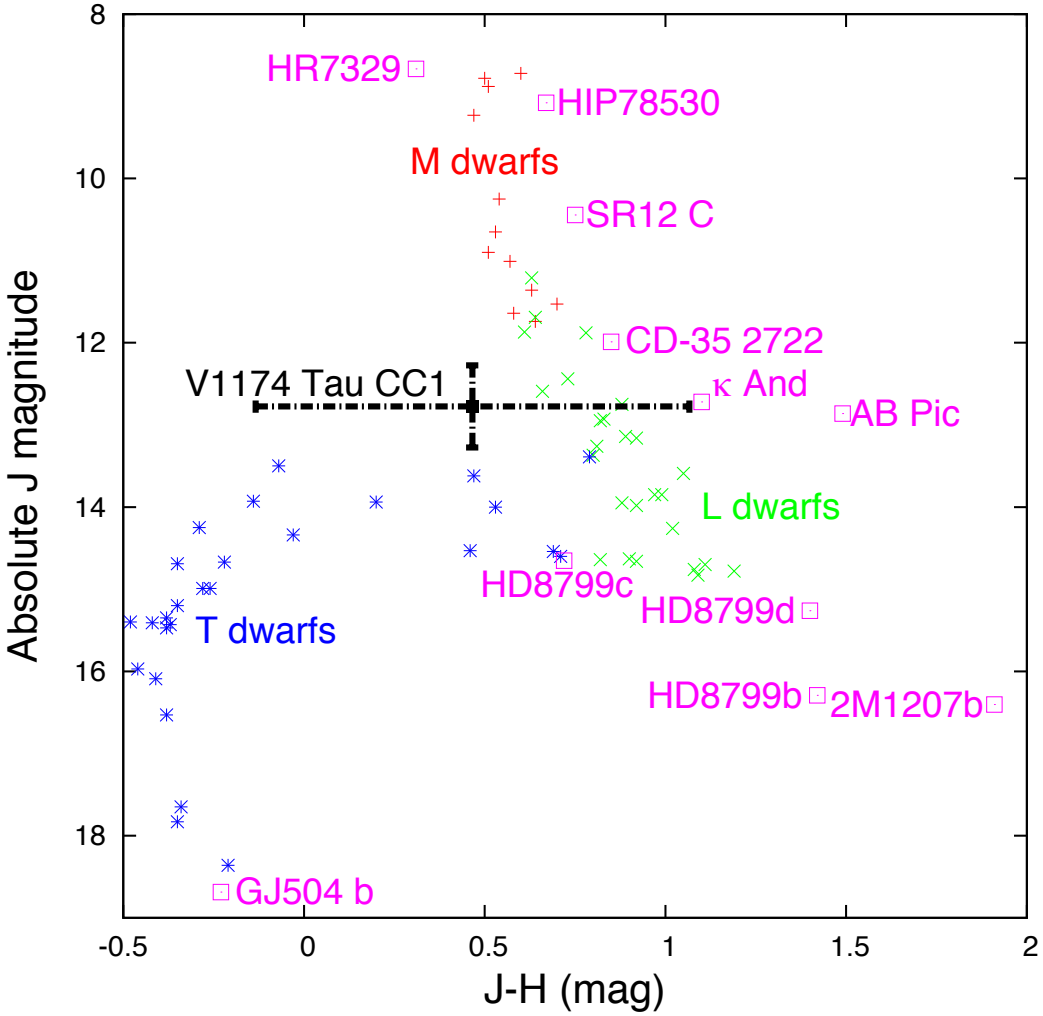

FIGURE 3.6: Color-Magnitude diagram for V1174 Tau CC1. Red, green, and blue dots represent the field M, L and T dwarfs (Leggett et al. 2010). 2M1207 b: Mohanty et al. (2007). HR 7329 b: Neuhäuser et al. (2011). SR12 C: Kuzuhara et al. (2011). HR8799 b, c, d: Marois et al. (2008). AB Pic: Bonnefoy et al. (2010). κ And: Carson et al. (2013b). HIP 78530: Lafrenière et al. (2011). CD-35 2722: Wahhaj et al. (2011). GJ504 b: Kuzuhara et al. (2013).

Chapter 4

Planet occurrence in the Pleiades

In this section, our observations are used to constrain the frequency of planets around a star. First, we define and calculate the detection efficiency $\varepsilon_{\rm n}$ as the probability of detecting a planet when star n hosts one gas-giant planet.

4.1 Method

We consider the separation range of planet detection in our HiCIAO/AO188 observations. The detection limit of a point source distant from the central star is determined solely from the total integration time, and is not affected by the stellar halo. As mentioned in Section 3.2, the detection limit of our observations (5σ) was 20.5 magnitudes with an integration time of 5–45 min beyond $1''.5$. However, the inner region ($< 1''.5$) contains residuals of the stellar halo, as seen in Figure 3.2 and Table 4.1. In this area, only brighter planets, brown dwarfs, and stars can be detected, but we are interested in the region where existing planets can be detected. The minimum separation for planet detection, which we define as the inner working angle (IWA), can depend not only on the sensitivity but also on the field rotation of ADI. By evaluating the suppression of the stellar halo in each target (Figure 3.2), we determined the IWA directly from the data as $0''.6$–$1''.0$. Nevertheless, the following discussion focuses on the outer region ($> 1''.5$), which is free from stellar halo effects. In the following calculation, $F_{\rm min}$ is defined as the minimum angular separation that permits detection of a planet with mass $M_{\rm P}$.

The H magnitude can be converted to planetary mass using the evolutionary model of Baraffe et al. (2003), assuming that Pleiades stars are 125 Myr old and 135 pc distant from Earth. This relationship gives the minimum detectable planetary mass $M_{\rm min}$ at each separation.

Next, we calculate the detection efficiency, which defines the probability that planets lie in the detectable parameter space of the observation. The detection efficiency $\varepsilon(M_{\rm P}, a, e)$ of finding a planet with a certain orbit in the Pleiades is derived from the planet mass $M_{\rm P}$, semi-major axis a, and eccentricity e. Here, we assume that a host star always supports one planet with the required orbital elements; a, e, inclination i (angle between line of sight and the orbital plane normal), and azimuth ϕ (angle between line of sight and periapsis). As the planet moves along its orbit, the separation angle F from the central star to the planet varies with the true anomaly θ as follows:

$$F = \frac{a\,(1-e^2)}{D\,(1+e\cos\theta)}\sqrt{\cos^2(\theta-\phi)\cos^2 i + \sin^2(\theta-\phi)}, \tag{4.1}$$

where D is the distance to the Pleiades cluster (D =135 pc). We then introduce $T_{\rm d}$, the time per orbital period $T_{\rm P}$ for which a planet of $M_{\rm P}$ is found within the range of $F \geqq F_{\rm min}$. In terms of $T_{\rm d}$, the detection efficiency of a certain orbit is given by $g(M_{\rm P}, a, e, i, \phi) = T_{\rm d}/T_{\rm P}$. Considering that the line of sight is randomly distributed and independent of planetary orbit, the detection efficiency of one orbit is

$$\varepsilon(M_{\rm P}, a, e) = \frac{\int_{i=-\pi/2}^{\pi/2}\sin i \int_{\phi=0}^{2\pi} g(M_{\rm P}, a, e, i, \phi)d\phi di}{\int_{i=-\pi/2}^{\pi/2}\sin i \int_{\phi=0}^{2\pi} d\phi di}. \tag{4.2}$$

Accordingly, the detection efficiency $\varepsilon_{\rm n}$ of a host star n is obtained from the distribution of planet masses, the semi-major axis, and eccentricity by

$$\varepsilon_{\rm n} = \frac{\int_{M_{\rm min}}^{M_{\rm max}}\frac{dN}{dM_{\rm P}}\int_{a_{\rm min}}^{a_{\rm max}}\frac{dN}{da}\int_0^1\frac{dN}{de}\varepsilon(M_{\rm P}, a, e)dM_{\rm P}dade}{\int_{M_{\rm min}}^{M_{\rm max}}\frac{dN}{dM_{\rm P}}\int_{a_{\rm min}}^{a_{\rm max}}\frac{dN}{da}\int_0^1\frac{dN}{de}dM_{\rm P}dade}. \tag{4.3}$$

Here, the important quantities are the number distribution of planet masses, the semi-major axis, and eccentricity, expressed as $dN/dM_{\rm P}$, dN/da and dN/de, respectively. The distribution of planet mass was derived as $dN/dM_{\rm P} \propto M_{\rm P}^{\alpha}, \alpha = -1.2$ to -1.9, from an RV survey of planets with orbital periods exceeding 100 days (Cumming et al. 2008). The same RV survey of planets with long orbital periods (shorter than 2000 days: Cumming et al. 2008) yielded distribution of the semi-major axis as $dN/da \propto a^{\beta}, \beta = -0.61$ or -1.0. Finally, the eccentricity distribution was derived as $dN/de \propto \exp(-4.2e)$, based on data in *The Extrasolar Planet Encyclopedia* [1]. These distributions are assumed in our following calculations.

[1] http://exoplanet.eu/

TABLE 4.1: Detection limits of observations

Name	N_{CC}[1]	Detection limit[2]			Efficiency
		H/K_S	Mass (M_J)		%
		mean	mean	min	
BD +22 574	2	20.8	9.5	8.4	83.4
HD 23912	1	21.0	8.9	7.9	92.8
V1171 Tau	3	20.1	9.5	9.4	81.7
HII 2462	-	19.6	10.7	9.4	35.2
HD 23863	-	20.6	9.7	8.9	57.5
HD 282954	1	21.1	8.7	7.8	90.1
HD 23514	1	21.2	8.4	7.3	94.0
HD 23247	1	20.4	9.7	9.4	76.7
V855 Tau	1	20.9	9.1	8.1	87.4
HD 24132	-	20.6	9.9	9.2	55.2
HD 23061	-	20.8	9.4	8.0	84.5
TYC 1800-2411-1	-	20.3	9.5	9.4	79.6
HII 1348	1	20.9	9.3	7.8	79.3
Melotte 22 SSHJ G214	-	21.1	8.8	7.6	96.7
BD +23 514	-	18.9	14.2	11.2	1.82
Melotte 22 SSHJ G213	-	21.6	7.5	6.2	99.1
Melotte 22 SSHJ G221	-	20.3	9.5	9.4	78.1
V1054 Tau	2	20.9	9.3	7.8	75.5
V1174 Tau	2	21.2	8.6	7.2	98.5
Melotte 22 SSHJ K101	-	20.4	9.5	9.1	95.6
Total	15	20.6	9.0	8.5	81.1[3]

[1] Number of companion candidates. [2] Magnitudes of detection limit are mean / minimum value beyond 1″5 in H/K_S band. Masses are linear interpolated based on COND03 (Baraffe et al. 2003) at 120 Myr. [3] BD +22 574 is excluded from mean.

Adopting Baraffe et al. (2003), the minimum detectable mass in our observations was 6–10 M_J at separations exceeding 1″.5 (Table 4.1). As shown in Figure 3.2, the IWAs of circular ($e = 0.0$) and eccentric orbits ($e = 0.9$) are 100 AU and 50 AU, respectively. Inserting this result into Equation (4.3), we find that the detection efficiency ε_n ranges from 50–99% for planets of mass of 9–13 M_J and semi-major axis of 50–1000 AU.

In the above discussion, we calculated the detection efficiency for one planet orbiting a single star, ε_n. We now consider the probability of detecting *at least* one planet, p_n, around a star n ($n = 1...N$). p_n is calculated from the detection efficiency ε_n and the number frequency of planets around a host star η, since

$$p_n = \eta \times \varepsilon_n. \tag{4.4}$$

As noted above, $\varepsilon_{\rm n}$ is uniquely determined by the orbital distribution of the planet and the detection separation range in the observations. On the other hand, $p_{\rm n}$ can be constrained by our imaging results for 20 stars. Therefore, we can constrain the planet frequency η around a host star.

In the following analysis, we employ Bayes' theorem as described by Vigan et al. (2012) and Lafrenière et al. (2007). The probability of detecting at least one planet is $\eta \times \varepsilon_{\rm n}$ while that of non-detection is $(1-\eta \times \varepsilon_{\rm n})$. Given $\varepsilon_{\rm n}$, the likelihood of the data is given by

$$L(\{d_{\rm n}\}|\eta) = \prod_{n=1}^{N} \left(1-\eta\varepsilon_{\rm n}\right)^{1-d_{\rm n}} \cdot \left(\eta\varepsilon_{\rm n}\right)^{d_{\rm n}}, \tag{4.5}$$

where $d_{\rm n}$ is a binary value that equals 1 if at least one planet is detected around a star n and 0 if no planet is detected. The set $\{d_{\rm n}\}$ on the left-hand side of Equation (4.5) contains the results of N observations. If no results are detected, the likelihood function follows a Poisson distribution:

$$\begin{aligned} L(\{d_{\rm n}\}|\eta) &= \prod_{n=1}^{N} \exp(-\eta\varepsilon_{\rm n}) && (4.6)\\ &= \exp\left(-\eta \sum_{n=1}^{N} \varepsilon_{\rm n}\right). && (4.7) \end{aligned}$$

From this likelihood function, the conditional probability distribution of a set of events $\{d_{\rm n}\}$ occuring with frequency η is

$$p\left(\eta|\{d_{\rm n}\}\right) = \frac{L(\{d_{\rm n}\}|\eta)p(\eta)}{\int_0^1 L(\{d_{\rm n}\}|\eta)p(\eta)d\eta}, \tag{4.8}$$

where p(η) is the prior probability of η. Since η is unknown a priori, $p(\eta) = 1$.

We define the cumulative distribution function CDF(η) of η as the probability of $H \leq \eta$,

$$\begin{aligned} \mathrm{CDF}(\eta) &= P(H \leq \eta) = \int_0^{\eta} p(H|\{d_{\rm n}\})dH && (4.9)\\ \mathrm{CDF}(0) &= 0 && (4.10)\\ \mathrm{CDF}(1) &= 1. && (4.11) \end{aligned}$$

The CDFs of two cases, no planet detected and one brown dwarf detected around a star, are plotted in Figure 4.1. The range of η can be formulated as a confidence

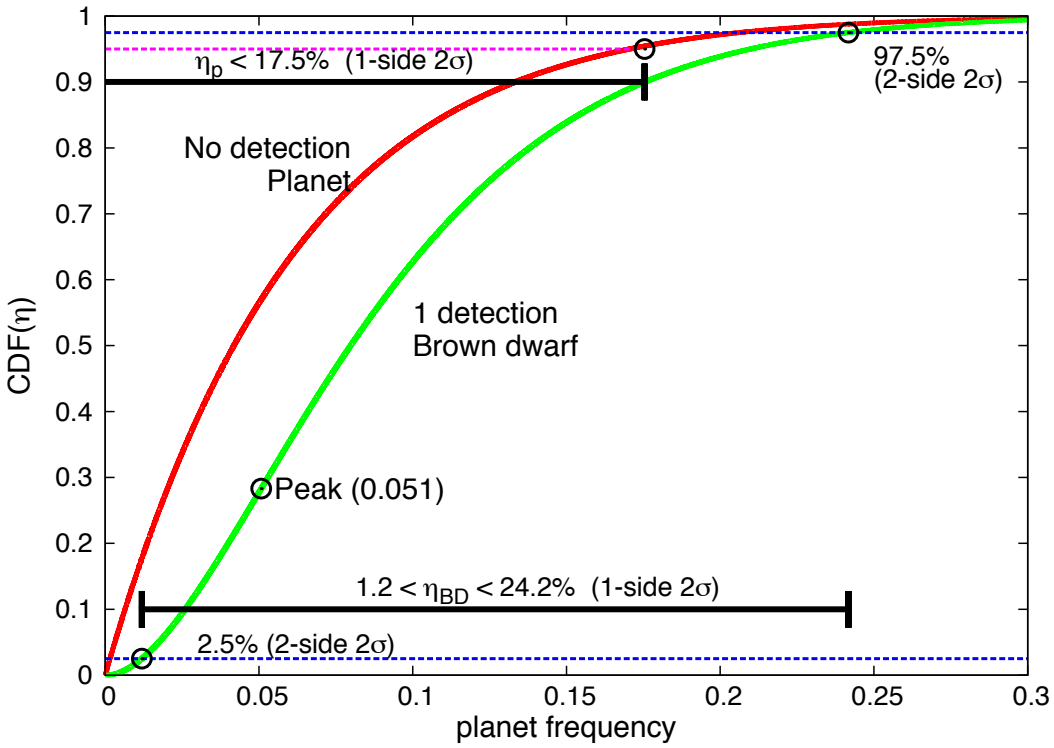

FIGURE 4.1: Cumulative distribution function of planet frequency CDF(η). Red and green line plot the CDF in the case of "no planet mass companion detected" and "one brown dwarf mass companion detected", respectively. The blue dotted lines indicate the upper and lower confidence limit at $2\sigma(95\%)$, and the magenta dotted line indicates the upper $2sigma$ confidence limit. The planet frequency ranges from 0–1.

interval (CI) on a given confidence level (CL) α,

$$\alpha = \int_{\eta_{\min}}^{\eta_{\max}} p\left(\eta|\{d_{\rm n}\}\right) d\eta, \tag{4.12}$$

where η_{max} and η_{min} are the maximum and minimum values of η respectively, in the set $\{d_{\rm n}\}$. The confidence level can also be described in terms of the CDF. For a two-sided 2 σ test ($\alpha = 0.95$), $\mathrm{CDF}(\eta_{\rm min}) = 0.025, and \mathrm{CDF}(\eta_{\rm max})$ =0.975; for a one-sided 2 σ test ($\alpha = 0.95$) , and $\mathrm{CDF}(\eta_{\rm max}) = 0.95$. If no planet is detected, the upper limit of the planet frequency $\eta_{\rm max}$ can be analytically computed from Equation 4.6 and 4.12,

$$\begin{aligned} \alpha = \mathrm{CDF}(\eta_{max}) &= \frac{\int_0^{\eta_{\max}} \exp\left(-\eta N \left\langle\varepsilon\right\rangle\right) d\eta}{\int_0^{1} \exp\left(-\eta N \left\langle\varepsilon\right\rangle\right) d\eta} \\ \eta_{\max} &= -\frac{\ln(1-\alpha)}{N \left\langle\varepsilon\right\rangle} \end{aligned} \tag{4.13}$$

where $N\langle\varepsilon\rangle = \sum_{n=1}^{N}(\varepsilon_{\rm n})$ and $N\langle\varepsilon\rangle \gg 1$.

No planetary mass companion candidates ($< 13\ M_{\rm J}$) were detected in our observations. Since no planets were found around our 20 target stars, the $\eta_{\rm max}$ was estimated at approximately 17.5% (CL = 95%) for planets in the 9–13 $M_{\rm J}$ mass range with semi-major axes of 50–1000 AU. The minimum $\eta_{\rm min}$ is always 0 in this case. If all parameters have been observed, or the stellar efficiencies of the 20 stars are 100%, Equation 4.13 gives the upper limit of frequency $\eta_{\rm max}$ as 14.98%.

4.2 Discussion

From observations of 20 stars, the upper limit (2σ) of the frequency of planets of masses 9–13 $M_{\rm J}$ orbiting at distances of 50–1000 AU from their host stars in the Pleiades (125 Myr, 135 pc) was estimated as 17.5%. Such a constraint has not previously been reported for star systems of a certain age (∼125 Myr).

In a previous direct imaging survey conducted by Lafrenière et al. (2007), the frequency of planets at mass and separation ranges of 0.5–13 $M_{\rm J}$ and 50–250 AU, respectively, was below 10%. These results were derived from observations of 85 stars by the Gemini North telescope. Similarly, the frequency of planets of mass $> 1\ M_{\rm J}$ separated at 40–500 AU was not greater than 9.3% (2σ) in VLT observations of 88 stars within 100 pc (Chauvin et al. 2010). Our estimate is consistent with these previous results, indicating that the planet frequency in the Pleiades is similar to that in other moving groups and around field stars.

According to these results, giant planets are very rare at larger separations (beyond approximately 50 AU), although a few candidate systems have been reported (*e.g.*, Itoh et al. 2005; Marois et al. 2008). Current formation theory predicts that heavy giant planets in distant regions can form only by disk instability. Thus, we speculate that such instabilities are not a major *in-situ* formation process for giant planets. Furthermore, our observations cover a wide area, extending beyond the typical size of protoplanetary disks (a few 100 AU; Andrews & Williams 2007). Planets are not expected to form *in situ* at such distances from their host star. However, it has been suggested that giant planets or their natal fragments in multiple planetary systems can be ejected into very wide orbits (10^2–10^5 AU) through gravitational interaction (Basu & Vorobyov 2012; Veras et al. 2009). At present, the observed rareness is consistent with theoretically predicted planet–planet scattering rates.

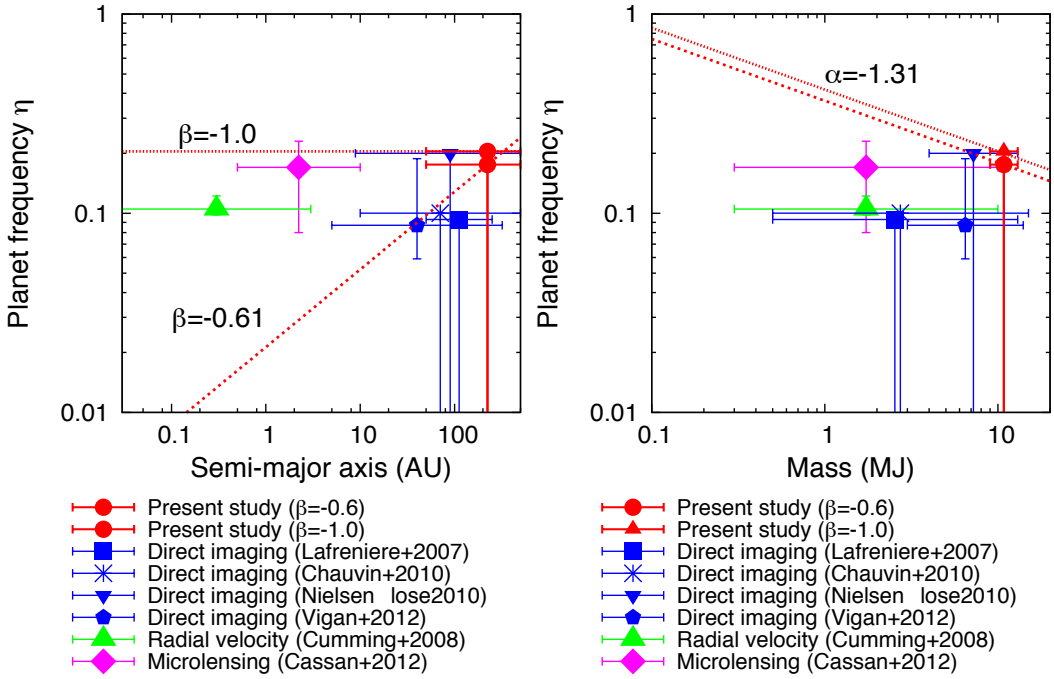

FIGURE 4.2: Planet frequency η as a function of semi-major axis (*left panel*) and planet mass (*right panel*). *Circles* indicate result from our work (50–1000 AU, 9–13 $M_{\rm J}$), while *squares* are the results of direct imaging (50–250 AU, 0.5–13 $M_{\rm J}$; Lafrenière et al. (2007)). *The star symbols*, *triangles* and *pentagons* indicate the results of other direct imaging studies; (10–500 AU, 0.5–15 $M_{\rm J}$; Chauvin et al. 2010), (8.9–911 AU, >4 $M_{\rm J}$; Nielsen & Close 2010) and (5–320 AU, 3–14 $M_{\rm J}$; Vigan et al. 2012), respectively. *Green triangles* denote the radial velocity (0.03–3 AU, 0.3–10 $M_{\rm J}$; Cumming et al. 2008), and *magenta diamonds* show microlensing results (0.5–10AU, 0.3–10 $M_{\rm J}$; Cassan et al. 2012). The dotted lines in both panels indicate the distribution of planet frequencies derived from our observations. The slopes of the lines in the *left* and *right* panels are −1.31 and −0.61, respectively.

In microlensing planetary surveys of the regions near host stars (OGLE: Beaulieu et al. (2006); Kubas et al. (2008), MOA: Sumi et al. (2010)), the frequency of planets of mass 0.3–10 $M_{\rm J}$ separated by 0.5–10 AU was 17^{+6}_{-9}% (Cassan et al. 2012). In addition, RV survey identified the frequency of planets more massive than 0.3–10 $M_{\rm J}$ over 0.03–3 AU as 10.5 ±1.7% (Cumming et al. 2008). Though the detectable separations in these other surveys differed from that in direct imaging, the frequency of planets derived from our survey appears similar to the frequencies derived from microlensing and RV surveys (Figure 4.2, Table 4.2).

We can also place limits on the frequency of brown dwarf mass companions in the Pleiades. The frequency of brown dwarfs (12–72$M_{\rm J}$, 28–1590 AU, $dN/dM \propto M^{-0.4}$) in 266 FGK was calculated as $3.2^{+7.3}_{-2.7}$% by Metchev & Hillenbrand (2009). In our study, we found brown dwarf companions around HII 1348, HD 23514 and

TABLE 4.2: Comparison of planet frequency observations.

Observation method	Ref.	Distribution index		Planet frequency (η) (%)
		Mass (α) $dN/dM_{\rm P} \propto (M_{\rm P})^{\alpha}$	Semi-major axis (β) $dN/da \propto a^{\beta}$	
Direct Imaging	Present work	-1.31	-0.61	≤ 17.5
		-1.31	-1.0	≤ 20.5
Direct Imaging	Lafrenière et al. (2007)	-1.2	-1.0	≤ 9.3
Direct Imaging	Chauvin et al. (2010)	-1.31	-0.61	≤ 10
Direct Imaging	Nielsen & Close (2010)	-1.31	-0.61	≤ 20
Direct Imaging	Vigan et al. (2012)	-1.31	-0.61	$8.7^{+10.1}_{2.8}$
Radial velocity	Cumming et al. (2008)	-1.31	-0.61	10.5 ± 1.7
Microlensing	Cassan et al. (2012)	-1.68	-1.0	17^{+6}_{-9}

β is used as described in Cumming et al. (2008). In direct imaging by Lafrenière et al. (2007), α and β were extrapolated from RV observations. Lafrenière et al. (2007) and Cassan et al. (2012) assumed a flat distribution in logarithmic semi-major axis space.

V1174 Tau. The companions around HD 23514 and V1174 Tau were not previous known at our target selection. However, the companion of HII 1348 was known at selection. Thus, using our result on two companions of the 19 stars (excluding HII 1348), we derived a companion brown dwarf frequency of $10.9^{+22.4}_{-7.7}$ (12–72$M_{\rm J}$, 50–500 AU, 2σ) in the Pleiades cluster, consistent with the result of Metchev & Hillenbrand (2009). On the other hands, Lodieu et al. (2012a) reported a *substellar binary* frequency of 25.6 ± 4.5 for stars of mass 30–75 $M_{\odot}$ smaller than $\sim$ 100–200 AU in the Pleiades. This suggests that the substellar *companion* frequency is lower than the substellar *binary* frequency in the Pleiades.

We detected point sources fainter than 14.5 mag around nine of the 20 target stars (40%), but whether these sources are real companion objects is unclear. At separations of 1″.5–10″, the detection limit is 20.5 mag in the H band. The possibility of finding other point sources is consistent with previous direct imaging studies with similar survey depth and FoV size. For instance, CCs were detected around 32 stars (44%) at a galactic latitude of $> |10°|$ in imaging study by Chauvin et al. (2010). Among these, five stars were confirmed as background objects while the proper motions of the remaining stars (78% of the sample) have yet to be observed. Most of them are probably background stars, but we would like to emphasize the potential utility of deep direct imaging in galactic modeling. Investigating this potential, however, is beyond the scope of this study.

Chapter 5

Summary

We conducted a SEEDS imaging survey for detection of extrasolar gas-giant planets in the Pleiades with the near-infrared imaging instrument HiCIAO and the adaptive optics instrument AO188 on the Subaru telescope between October 2009 and December 2012. ADI observations identified 15 companion candidates around 10 host stars in the H and $K_{\rm S}$ bands. The detection limit of our observations (5σ) was 20.6 magnitudes beyond $1''.5$ with an integration time of 5–45 min. HD 23514 and HII 1348 were each accompanied by a brown dwarf companion, consistent with previously reported analyses of proper motion measurements (Geißler et al. 2012; Rodriguez et al. 2012). A stellar mass ($> 100 M_{\rm J}$) companion might accompany HD 23247. Eight of the 15 candidates were confirmed as background stars based on their of proper motions. One candidate was absent in the second epoch observation; thus, was unlikely to be a background or companion object. Another candidate could not be confirmed or otherwise as a background star, on account of its imprecise proper motion. The remaining two candidates are most likely to be co-moving companions around V1174 Tau. With H magnitudes of 18.0 and 18.5 respectively, both candidates may have brown dwarf mass. If confirmed, these companions would be the lowest mass companions reported in the Pleiades.

Based on the detection limit of our equipment, we determined the detection efficiency, defined as the probability of finding a 9–13 Jovian-mass planet at 50–1000 AU from its host star in the Pleiades, as about 80%. Since no such planets were detected, we estimated the frequency of stars supporting gas-giant planets in the Pleiades is less than 17.5%. This result is consistent with previous direct imaging studies, indicating that planet frequency in the Pleiades is not considerably higher than the frequency in moving groups and field stars.

Acknowledgements

My heartfelt appreciation goes to Professor Dr. Hiroshi Shibai at Osaka University who offered continuing support and constant encouragement throughout my 7-year-old laboratory assignment. Without his guidance and persistent help this thesis would not have been possible. My work on the development of the *Far-Infrared Interferometry Experiment* (FITE) is also supported by him.

I am also indebted to Assistant Professor Dr. Misato Fukagawa whose meticulous comments greatly assited my study. Associate Professor Dr. Takahiro Sumi provided insightful comments and suggestions. I would also like to express my gratitude to my family for their moral support and warm encouragements.

I would like to greatly thank *Strategic Exploration of Exoplanets and Disks with Subaru* (SEEDS)-OC members, including Special Purpose Associate Professor Dr. Taro Matsuo at Kyoto University, for their support and comment. I have collaborated with them in discussion and study to produce this work. Other SEEDS members such as Professor Motohide Tamura at Tokyo University, provided observational opportunity and valuable datas, for which I am most grateful.

I would like to offer my special thanks to past and present members of the *Infrared Astronomy Laboratory* of Osaka University and *U-lab.* of Nagoya University.

References

Allard, F., Hauschildt, P. H., & Schweitzer, A. 2000, ApJ, 539, 366

An, D., Terndrup, D. M., Pinsonneault, M. H., et al. 2007, ApJ, 655, 233

Andrews, S. M., & Williams, J. P. 2007, ApJ, 659, 705

Balog, Z., Kiss, L. L., Vinkó, J., et al. 2009, ApJ, 698, 1989

Baraffe, I., Chabrier, G., Allard, F., & Hauschildt, P. H. 1998, A&A, 337, 403

—. 2002, A&A, 382, 563

Baraffe, I., Chabrier, G., Barman, T. S., Allard, F., & Hauschildt, P. H. 2003, A&A, 402, 701

Barrado Y Navascues, D., Stauffer, J. R., Briceno, C., et al. 2001, VizieR Online Data Catalog, 213, 40103

Barrado y Navascués, D., Stauffer, J. R., & Jayawardhana, R. 2004, ApJ, 614, 386

Basu, S., & Vorobyov, E. I. 2012, ApJ, 750, 30

Batalha, N. M., Rowe, J. F., Bryson, S. T., et al. 2013, ApJS, 204, 24

Bean, J. L., Miller-Ricci Kempton, E., & Homeier, D. 2010, Nature, 468, 669

Beaulieu, J.-P., Bennett, D. P., Fouqué, P., et al. 2006, Nature, 439, 437

Belikov, A. N., Hirte, S., Meusinger, H., Piskunov, A. E., & Schilbach, E. 1998, A&A, 332, 575

Belikov, A. N., Kharchenko, N. V., Piskunov, A. E., et al. 2002, A&A, 384, 145

Biller, B. A., Close, L. M., Masciadri, E., et al. 2007, ApJS, 173, 143

Bonfils, X., Delfosse, X., Udry, S., et al. 2013, A&A, 549, A109

Bonnefoy, M., Chauvin, G., Rojo, P., et al. 2010, A&A, 512, A52

Bouvier, J., Rigaut, F., & Nadeau, D. 1997, A&A, 323, 139

Cameron, A. G. W. 1978, Moon and Planets, 18, 5

Carson, J., Thalmann, C., Janson, M., et al. 2013a, ApJ, 763, L32

—. 2013b, ApJ, 763, L32

Cassan, A., Kubas, D., Beaulieu, J.-P., et al. 2012, Nature, 481, 167

Chabrier, G., & Baraffe, I. 2000, ARA&A, 38, 337

Charbonneau, D., Brown, T. M., Latham, D. W., & Mayor, M. 2000, ApJ, 529, L45

Chauvin, G., Lagrange, A.-M., Dumas, C., et al. 2004, A&A, 425, L29

Chauvin, G., Lagrange, A.-M., Bonavita, M., et al. 2010, A&A, 509, A52

Cumming, A., Butler, R. P., Marcy, G. W., et al. 2008, PASP, 120, 531

Currie, T., Burrows, A., Itoh, Y., et al. 2011, ApJ, 729, 128

Dobbie, P. D., Lodieu, N., & Sharp, R. G. 2010, MNRAS, 409, 1002

Dong, S., DePoy, D. L., Gaudi, B. S., et al. 2006, ApJ, 642, 842

D'Orazi, V., & Randich, S. 2009, A&A, 501, 553

Fischer, D. A., & Valenti, J. 2005, ApJ, 622, 1102

Ford, A., Jeffries, R. D., & Smalley, B. 2005, MNRAS, 364, 272

Fortney, J. J., Marley, M. S., Hubickyj, O., Bodenheimer, P., & Lissauer, J. J. 2005, Astronomische Nachrichten, 326, 925

Fortney, J. J., Marley, M. S., Saumon, D., & Lodders, K. 2008, ApJ, 683, 1104

Freistetter, F., Krivov, A. V., & Löhne, T. 2007, A&A, 466, 389

Fressin, F., Torres, G., Charbonneau, D., et al. 2013, ApJ, 766, 81

Garcia, B., Hernandez, C., Malaroda, S., Morrell, N., & Levato, H. 1988, Ap&SS, 148, 163

Geißler, K., Metchev, S. A., Pham, A., et al. 2012, ApJ, 746, 44

Gratton, R. 2000, in Astronomical Society of the Pacific Conference Series, Vol. 198, Stellar Clusters and Associations: Convection, Rotation, and Dynamos, ed. R. Pallavicini, G. Micela, & S. Sciortino, 225

Hayano, Y., Takami, H., Oya, S., et al. 2010, in Society of Photo-Optical Instrumentation Engineers (SPIE) Conference Series, Vol. 7736, Society of Photo-Optical Instrumentation Engineers (SPIE) Conference Series

Heinze, A. N., Hinz, P. M., Sivanandam, S., et al. 2010, ApJ, 714, 1551

Henry, G. W., Marcy, G. W., Butler, R. P., & Vogt, S. S. 2000, ApJ, 529, L41

Hodapp, K. W., Suzuki, R., Tamura, M., et al. 2008, in Society of Photo-Optical Instrumentation Engineers (SPIE) Conference Series, Vol. 7014, Society of Photo-Optical Instrumentation Engineers (SPIE) Conference Series

Howard, A. W., Marcy, G. W., Bryson, S. T., et al. 2012, ApJS, 201, 15

Ida, S., & Lin, D. N. C. 2004, ApJ, 604, 388

—. 2005, ApJ, 626, 1045

Inutsuka, S.-i., Machida, M. N., & Matsumoto, T. 2010, ApJ, 718, L58

Itoh, Y., Oasa, Y., Funayama, H., et al. 2011, Research in Astronomy and Astrophysics, 11, 335

Itoh, Y., Hayashi, M., Tamura, M., et al. 2005, ApJ, 620, 984

Janson, M., Bonavita, M., Klahr, H., & Lafrenière, D. 2012, ApJ, 745, 4

Kiraga, M., & Paczynski, B. 1994, ApJ, 430, L101

Kouwenhoven, M. B. N., Goodwin, S. P., Parker, R. J., et al. 2010, MNRAS, 404, 1835

Kratter, K. M., Murray-Clay, R. A., & Youdin, A. N. 2010, ApJ, 710, 1375

Kraus, A. L., & Hillenbrand, L. A. 2007, AJ, 134, 2340

Kubas, D., Cassan, A., Dominik, M., et al. 2008, A&A, 483, 317

Kuiper, G. P. 1951, Proceedings of the National Academy of Science, 37, 1

Kuzuhara, M., Tamura, M., Ishii, M., et al. 2011, AJ, 141, 119

Kuzuhara, M., Tamura, M., Kudo, T., et al. 2013, ApJ, 774, 11

Lafrenière, D., Jayawardhana, R., Janson, M., et al. 2011, ApJ, 730, 42

Lafrenière, D., Doyon, R., Marois, C., et al. 2007, ApJ, 670, 1367

Lagrange, A.-M., Gratadour, D., Chauvin, G., et al. 2009, A&A, 493, L21

Lagrange, A.-M., Bonnefoy, M., Chauvin, G., et al. 2010, Science, 329, 57

Lawrence, A., Warren, S. J., Almaini, O., et al. 2013, VizieR Online Data Catalog, 2319, 0

Leconte, J., Soummer, R., Hinkley, S., et al. 2010, ApJ, 716, 1551

Leggett, S. K., Burningham, B., Saumon, D., et al. 2010, ApJ, 710, 1627

Liu, M. C. 2004, Science, 305, 1442

Lodieu, N., Deacon, N. R., & Hambly, N. C. 2012a, MNRAS, 422, 1495

Lodieu, N., Deacon, N. R., Hambly, N. C., & Boudreault, S. 2012b, MNRAS, 426, 3403

Lodieu, N., Dobbie, P. D., Deacon, N. R., et al. 2007, MNRAS, 380, 712

Maccone, C. 2012, in Mathematical SETI, Springer Praxis Books (Springer Berlin Heidelberg), 3–72

Makarov, V. V. 2006, AJ, 131, 2967

Marley, M. S., Fortney, J. J., Hubickyj, O., Bodenheimer, P., & Lissauer, J. J. 2007, ApJ, 655, 541

Marois, C., Lafrenière, D., Doyon, R., Macintosh, B., & Nadeau, D. 2006, ApJ, 641, 556

Marois, C., Macintosh, B., Barman, T., et al. 2008, Science, 322, 1348

Marois, C., Zuckerman, B., Konopacky, Q. M., Macintosh, B., & Barman, T. 2010, Nature, 468, 1080

Masciadri, E., Mundt, R., Henning, T., Alvarez, C., & Barrado y Navascués, D. 2005, ApJ, 625, 1004

Masset, F. S., & Papaloizou, J. C. B. 2003, ApJ, 588, 494

Matsuo, T., Shibai, H., Ootsubo, T., & Tamura, M. 2007, ApJ, 662, 1282

Mayor, M., & Queloz, D. 1995, Nature, 378, 355

Mayor, M., Marmier, M., Lovis, C., et al. 2011, ArXiv e-prints, arXiv:1109.2497

Mazeh, T., Naef, D., Torres, G., et al. 2000, ApJ, 532, L55

Metchev, S., Marois, C., & Zuckerman, B. 2009, ApJ, 705, L204

Metchev, S. A., & Hillenbrand, L. A. 2009, ApJS, 181, 62

Micela, G., Sciortino, S., Kashyap, V., Harnden, Jr., F. R., & Rosner, R. 1996, ApJS, 102, 75

Mizuno, H. 1980, Progress of Theoretical Physics, 64, 544

Mohanty, S., Jayawardhana, R., Huélamo, N., & Mamajek, E. 2007, ApJ, 657, 1064

Moraux, E., Bouvier, J., Stauffer, J. R., Barrado y Navascués, D., & Cuillandre, J.-C. 2007, A&A, 471, 499

Mouillet, D., Larwood, J. D., Papaloizou, J. C. B., & Lagrange, A. M. 1997, MNRAS, 292, 896

Narita, N., Fukui, A., Ikoma, M., et al. 2013, ApJ, 773, 144

Netopil, M., & Paunzen, E. 2013, A&A, 557, A10

Neuhäuser, R., Ginski, C., Schmidt, T. O. B., & Mugrauer, M. 2011, MNRAS, 416, 1430

Nielsen, E. L., & Close, L. M. 2010, ApJ, 717, 878

Okamoto, Y. K., Kataza, H., Honda, M., et al. 2004, Nature, 431, 660

Perryman, M. A. C., Brown, A. G. A., Lebreton, Y., et al. 1998, A&A, 331, 81

Pinfield, D. J., Dobbie, P. D., Jameson, R. F., et al. 2003, MNRAS, 342, 1241

Pöhnl, H., & Paunzen, E. 2010, A&A, 514, A81

Pollack, J. B., Hubickyj, O., Bodenheimer, P., et al. 1996, Icarus, 124, 62

Raboud, D., & Mermilliod, J.-C. 1998, A&A, 329, 101

Rafikov, R. R. 2007, ApJ, 662, 642

—. 2011, ApJ, 727, 86

Rameau, J., Chauvin, G., Lagrange, A.-M., et al. 2013, A&A, 553, A60

Rein, H. 2012, ArXiv e-prints, arXiv:1211.7121

Rodriguez, D. R., Marois, C., Zuckerman, B., Macintosh, B., & Melis, C. 2012, ApJ, 748, 30

Sagan, C. 1983, Cosmos, Vol. 1 (Random House, New York)

Saumon, D., Hubbard, W. B., Burrows, A., et al. 1996, ApJ, 460, 993

Skiff, B. A. 2009, VizieR Online Data Catalog, 1, 2023

Soderblom, D. R., Laskar, T., Valenti, J. A., Stauffer, J. R., & Rebull, L. M. 2009, AJ, 138, 1292

Soderblom, D. R., Nelan, E., Benedict, G. F., et al. 2005, AJ, 129, 1616

Spiegel, D. S., & Burrows, A. 2012, ApJ, 745, 174

Stauffer, J. R., Schultz, G., & Kirkpatrick, J. D. 1998, ApJ, 499, L199

Stauffer, J. R., Hartmann, L. W., Fazio, G. G., et al. 2007, ApJS, 172, 663

Sumi, T., Bennett, D. P., Bond, I. A., et al. 2010, ApJ, 710, 1641

Sumi, T., Kamiya, K., Bennett, D. P., et al. 2011, Nature, 473, 349

Sumi, T., Bennett, D. P., Bond, I. A., et al. 2013, ApJ, 778, 150

Suzuki, R., Kudo, T., Hashimoto, J., et al. 2010, in Society of Photo-Optical Instrumentation Engineers (SPIE) Conference Series, Vol. 7735, Society of Photo-Optical Instrumentation Engineers (SPIE) Conference Series

Tamura, M. 2009, in American Institute of Physics Conference Series, Vol. 1158, American Institute of Physics Conference Series, ed. T. Usuda, M. Tamura, & M. Ishii, 11–16

van der Marel, R. P., Gerssen, J., Guhathakurta, P., Peterson, R. C., & Gebhardt, K. 2002, AJ, 124, 3255

van Leeuwen, F. 2009, A&A, 497, 209

Veras, D., Crepp, J. R., & Ford, E. B. 2009, ApJ, 696, 1600

Vigan, A., Patience, J., Marois, C., et al. 2012, A&A, 544, A9

Wahhaj, Z., Liu, M. C., Biller, B. A., et al. 2011, ApJ, 729, 139

Winn, J. N., Noyes, R. W., Holman, M. J., et al. 2005, ApJ, 631, 1215

Wright, C. O., Egan, M. P., Kraemer, K. E., & Price, S. D. 2003, AJ, 125, 359

Wright, J. T., & Gaudi, B. S. 2013, Exoplanet Detection Methods, ed. T. D. Oswalt, L. M. French, & P. Kalas (Springer Netherlands), 489

Wright, J. T., Marcy, G. W., Howard, A. W., et al. 2012, ApJ, 753, 160

Yamamoto, K., Matsuo, T., Shibai, H., et al. 2013, PASJ, 65, 90

Zacharias, N., Monet, D. G., Levine, S. E., et al. 2004, in Bulletin of the American Astronomical Society, Vol. 36, American Astronomical Society Meeting Abstracts, 1418

List of Publications

1. Referred Paper

1. Yamamoto, K., Matsuo, T., Shibai, H., Itoh, Y., Konishi, M., Sudo, J., Tanii, R., Fukagawa, M., Sumi, T., Kudo, T., Hashimoto, J., Kusakabe, N., Abe, L., Brandner, W., Brandt, T. D., Carson, J., Currie, T., Egner, S. E., Feldt, M., Goto, M., Grady, C., Guyon, O., Hayano, Y., Hayashi, M., Hayashi, S., Henning, T., Hodapp, K., Ishii, M., Iye, M., Janson, M., Kandori, R., Knapp, G. R., Kuzuhara, M., Kwon, J., McElwain, M., Miyama, S., Morino, J-I., Moro-Martin, A., Nishikawa, J., Nishimura, T., Pyo, T-S., Serabyn, E., Suto, H., Suzuki, R., Takami, M., Takato, N., Terada, H., Thalmann, C., Tomono, D., Turner, E. L., Wisniewski, J., Watanabe, M., Yamada, T., Takami, H., & Usuda, T., 2013, "Direct Imaging Search for Extrasolar Planets in the Pleiades", Publications of the Astronomical Society of Japan, 65, 4, 90, 19

2. Nakashima, A., Shibai, H., Kawada, M., Matsuo, T., Narita, M., Kato, E., Kanoh, T., Kohyama, T., Matsumoto, Y., Morishita, H., Watabe, T., Yamamoto, K., Tanabe, M., Kanoh, R., & Itoh, Y. 2011, "Far-Infrared Interferometric Telescope Experiment (FITE): Three-Axis Stabilized Attitude Control System", Transactions of the Japanese Society for Artificial Intelligence, Aerospace Technology Japan, 8, Tm_19

3. Kato, E., Shibai, H., Kawada, M., Narita, M., Matsuo, T., Ohkubo, A., Suzuki, M., Kanoh, T., Yamamoto, K., & FITE Team 2010, "Far-Infrared Interferometric Telescope Experiment : I. Interferometer Optics", Transactions of Space Technology Japan, 7, Tm_47

2. Conference Proceedings

1. Yamamoto, K., Matsuo, T., McElwain, M., Tamura, M., Morishita, H., Nakashima, A., Shibai, H., Fukagawa, M., Kato, E., Kanoh, T., Itoh, Yusuke,

Kaneko, Y., Shimoura, M., Itoh, Yoichi, Funayama, H., & Hashiguchi, T. Exoplanets and Disks: Their Formation and Diversity, The 2nd Subaru International Conference, Hawaii, 9-12 March 2009. p. 273

2. Sasaki, A., Shibai, H., Sumi, T., Fukagawa, M., Kanoh, T., Yamamoto, K., Itoh, Y., Aimi, Y., Kuwada, Y., Kaneko, Y., Konishi, M., Sai, S., Akiyama, N., & Narita, M. 2012, "Development of new optical adjustment system for FITE (Far-Infrared Interferometric Telescope Experiment)", Optical and Infrared Interferometry III. Proceedings of the SPIE, Volume 8445, 84452Z, 9

3. Shibai, H., Fukagawa, M., Kato, E., Kanoh, T., Kohyama, T., Itoh, Y., Yamamoto, K., Kawada, M., Watabe, T., Nakashima, A., Tanabe, M., Kanoh, R., & Narita, M. "Far-Infrared Interferometric Experiment (FITE): Toward the First Flight", Pathways Towards Habitable Planets, proceedings of a workshop held 14 to 18 September 2009 in Barcelona, Spain. Edited by Vincent Coudè du Foresto, Dawn M. G., & Ignasi R. San Francisco: Astronomical Society of the Pacific, p.541

4. Kanoh, T., Shibai, H., Fukagawa, M., Matsuo, T., Kato, E., Itoh, Y., Kawada, M., Watabe, T., Kohyama, T., Matsumoto, Y., Morishita, H., Yamamoto, K., Kanoh, R., Nakashima, A., Tanabe, M., & Narita, M. "Development of the Far-Infrared Interferometric Telescope Experiment", Exoplanets and Disks: Their Formation and Diversity, The 2nd Subaru International Conference, Hawaii, 9-12 March 2009. p. 389

5. Kohyama, T., Shibai, H., Mitsunobu, K., Watabe, T., Matsuo, T., Ohkubo, A., Katoh, E., Kanoh, T., Suzuki, M., Mochizuki, S., Matsumoto, Y., Morishita, H., Yamamoto, K., Kanoh, R., Nakashima, A., Tanabe, M., Doi, Y., Narita, M., 2008, "Far-Infrared Interferometric Telescope Experiment (FITE): Sensor Optics", Optical and Infrared Interferometry. Edited by Schöller, M., Danchi, W. C.; Delplancke, F. Proceedings of the SPIE, Volume 7013, pp. 70133O-70133O-10

6. 芝井 広、 住 貴宏、 深川美里、 叶 哲生、 伊藤優佑、 山本広大、 會見有香子、くわ田嘉大、 小西美穂子、 佐々木彩奈、 秋山直輝、 成田正直、 吉田哲也、 斉藤芳隆 "宇宙遠赤外線干渉計（FITE）プロジェクト:次回フライトに向けて" 、大気球シンポジウム、JAXA/ISAS、10 月、2012、p. 32

7. 叶 哲生、 芝井 広、 住 貴宏、 深川美里、 伊藤優佑、 山本広大、 會見有香子、金子有紀、 くわ田嘉大、 小西美穂子、 蔡 承亨、 佐々木彩奈、 成田正

直、 吉田哲也、 斉藤芳隆、 田村啓輔 “気球搭載遠赤外線干渉計 FITE 次回フライト計画” 、大気球シンポジウム、JAXA/ISAS 、10 月、2011 、 p.10

8. 叶 哲生、芝井 広、深川美里、加藤恵理、幸山常仁、伊藤優佑、山本広大 、金子有紀、下浦美那、會見有香子、くわ田嘉大、Dimitrios Kontopoulos 、渡部豊喜、松尾太郎、川田光伸、成田正直 “遠赤外線干渉計 FITE のフライト計画” 、大気球シンポジウム、JAXA/ISAS 、9 月、2010 、p. 96

9. 叶 哲生、芝井 広、松尾太郎、加藤恵理、伊藤優佑、川田光伸、幸山常仁、松本有加、森下祐乃、狩野良子、田辺光弘、中島亜紗美、山本広大 、渡部豊喜、成田正直、土井靖生 “遠赤外線干渉計 FITE の地上試験と観測計画” 、大気球シンポジウム、JAXA/ISAS 、9 月、2008 、p. 61

List of Presentations

1. Oral Presentation

1. 山本広大、松尾太郎、芝井 広、住 貴宏、深川美里、小西美穂子、須藤 淳、Matthias S. Samland、伊藤洋一、田村元秀、HiCIAO/AO188/Subaru チーム “SEEDS による散開星団での系外惑星探査 4” 、日本天文学会秋季年会、東北大学、9 月、2013 、P221a

2. 山本広大、松尾太郎、芝井 広、深川美里、小西美穂子、須藤 淳、伊藤洋一、谷井良子、田村元秀、HiCIAO/AO188/Subaru チーム “SEEDS による散開星団での系外惑星探査 3” 、日本天文学会秋季年会、大分大学、9 月、2012 、P203a

3. 山本広大、松尾太郎、芝井 広、深川美里、小西美穂子、伊藤洋一、谷井良子、田村元秀、HiCIAO/AO188/Subaru teams “SEEDS による散開星団での系外惑星探査２” 、日本天文学会秋季年会、鹿児島大学、9 月、2011 、P67a

4. 山本広大、松尾太郎、芝井 広、深川美里、叶 哲生、伊藤優佑、下浦美那、くわ田嘉大、伊藤洋一、谷井良子、田村元秀、中島亜紗美、HiCIAO/AO188/Subaru teams “SEEDS による散開星団での系外惑星探査” 、日本天文学会秋季年会、金沢大学、9 月、2010 、P55a

5. 山本広大、松尾太郎、M. McElwain、田村元秀、森下裕乃、中島亜紗美、芝井広、深川美里、加藤恵理、叶 哲生、伊藤優佑、金子有紀、下浦美那、伊藤洋一、船山日斗志、橋口敏郎 “SEEDS：散開星団、Moving group における惑星検出確率の導出” 、日本天文学会春季年会、大阪府立大学、3 月、2009 、P55a

6. Samland M. S., Matsuo T., Shibai H., Yamamoto K., Konishi M., Sudo J., Fukagawa M., Sumi T., HiCIAO/AO188/Subaru Team “SEEDS Direct Imaging Survey of Ursa Major Members” 、日本天文学会秋季年会、東北大学、9 月、2013 、P222a

7. 小西美穂子、芝井 広、松尾太郎、住 貴宏、深川美里、山本広大、須藤 淳、Matthias S. Samland、SEEDS/HiCIAO/AO188 チーム “太陽系外惑星探査における恒星混入率の導出：赤外線深撮像観測を用いた銀河系恒星分布モデルへの制限” 、日本天文学会秋季年会、東北大学、9 月、2013 、P223a

8. 小西美穂子、松尾太郎、芝井 広、深川美里、山本広大、須藤 淳、伊藤洋一、谷井良子、HiCIAO/AO188/Subaru チーム “直接撮像による系外惑星探査における二種類の解析方法の比較” 、日本天文学会秋季年会、大分大学、9 月、2012 、V222a

9. 小西美穂子、松尾太郎、芝井 広、深川美里、山本広大、伊藤洋一、谷井良子、HiCIAO/AO188/Subaru teams “SEEDS における系外惑星探査のための画像評価方法の開発” 、日本天文学会秋季年会、鹿児島大学、9 月、2011 、P68a

10. 芝井 広、松尾太郎、加藤恵理、叶 哲生、伊藤優佑、川田光伸、渡部豊喜、幸山常仁、松本有加、森下祐乃、狩野良子、田邊光弘、中島亜紗美、山本広大、吉田哲也、斉藤芳隆、成田正直、Antonio Mario Magalhaes, Jose Williams Vilas-Boas “気球搭載遠赤外線干渉計 FITE：ファーストフライト準備”、日本天文学会春季年会、大阪府立大学、3 月、2009 、W07a

11. 叶 哲生、芝井 広、松尾太郎、加藤恵理、伊藤優佑、川田光伸、渡部豊喜、幸山常仁、松本有加、森下祐乃、狩野良子、田邊光弘、中島亜紗美、山本広大、成田正直 “気球搭載遠赤外線干渉計 FITE：干渉光学系の性能評価” 、日本天文学会春季年会、大阪府立大学、3 月、2009 、W08a

12. 松本有加、渡部豊喜、芝井 広、松尾太郎、加藤恵理、叶 哲生、伊藤優佑、川田光伸、幸山常仁、森下祐乃、狩野良子、田邊光弘、中島亜紗美、山本広大、成田正直 “気球搭載遠赤外線干渉計 FITE：中間赤外線検出器” 、日本天文学会春季年会、大阪府立大学、3 月、2009 、W09a

13. 中島亜紗美、芝井 広、松尾太郎、加藤恵理、叶 哲生、伊藤優佑、川田光伸、渡部豊喜、幸山常仁、松本有加、森下祐乃、狩野良子、田邊光弘、山本広大、成田正直 “気球搭載遠赤外線干渉計 FITE：3 軸姿勢制御システム” 、日本天文学会春季年会、大阪府立大学、3 月、2009 、W10a

14. 加藤恵理、芝井 広、川田光伸、渡部豊喜、大坪貴文、松尾太郎、大久保篤史、叶 哲生、鈴木未来、望月 駿、幸山常仁、松本有加、森下祐乃、山本広大、狩野良子、田邊光弘、中島亜紗美、土井靖生、成田正直 “気球搭載遠赤外線干渉計 FITE: 干渉光学系” 、日本天文学会春季年会、国立オリンピック記念青少年総合センター、3 月、2008 、W63a

15. 叶 哲生、芝井 広、川田光伸、渡部豊喜、大坪貴文、松尾太郎、大久保篤史、加藤恵理、鈴木未来、望月 駿、幸山常仁、松本有加、森下祐乃、山本広大、狩野良子、田邊光弘、中島亜紗美、土井靖生、成田正直 “気球搭載遠赤外線干渉計 FITE: 光学系調整機構” 、日本天文学会春季年会、国立オリンピック記念青少年総合センター、3 月、2008 、W64a

16. 鈴木未来、芝井 広、川田光伸、渡部豊喜、大坪貴文、松尾太郎、大久保篤史、加藤恵理、叶 哲生、望月 駿、幸山常仁、松本有加、森下祐乃、山本広大、狩野良子、田邊光弘、中島亜紗美、土井靖生、成田正直 “気球搭載遠赤外線干渉計 FITE: 構造系” 、日本天文学会春季年会、国立オリンピック記念青少年総合センター、3 月、2008 、W65a

17. 幸山常仁、芝井 広、川田光伸、渡部豊喜、大坪貴文、松尾太郎、大久保篤史、加藤恵理、叶 哲生、鈴木未来、望月 駿、松本有加、森下祐乃、山本広大、狩野良子、田邊光弘、中島亜紗美、土井靖生、成田正直 “気球搭載遠赤外線干渉計 FITE: 極低温光学系の開発” 、日本天文学会春季年会、国立オリンピック記念青少年総合センター、3 月、2008 、W66a

18. 森下祐乃、芝井 広、川田光伸、渡部豊喜、大坪貴文、松尾太郎、大久保篤史、加藤恵理、叶 哲生、鈴木未来、望月 駿、幸山常仁、松本有加、山本広大、狩野良子、田邊光弘、中島亜紗美、土井靖生、成田正直 “気球搭載遠赤外線干渉計 FITE: 構造系” 、日本天文学会春季年会、国立オリンピック記念青少年総合センター、3 月、2008 、W67a

2. Poster Presentation

1. 山本広大、 松尾太郎、芝井 広、深川美里、小西美穂子、須藤 淳、伊藤洋一、谷井良子 “Search for Extrasolar planets in the Pleiades Open Cluster with HiCIAO/AO188” 、第 8 回 太陽系外惑星大研究会、4 月、2012

2. 山本広大、松尾太郎、芝井 広、深川美里、加藤恵理、叶 哲生、伊藤優佑、下浦美那、くわ田嘉大、伊藤洋一、橋口敏郎、中島亜紗美、田村元秀、HiCIAO/AO188/Subaru teams “SEEDS による散開星団の系外惑星探査” 、日本天文学会春季年会、広島大学、3 月、2010 、P40b

3. 佐々木彩奈、芝井 広、叶 哲生、伊藤優佑、山本広大、秋山直輝、住 貴宏、深川美里、會見有香子、桑田嘉大、小西美穂子、成田正直 “遠赤外線干渉計 FITE の新干渉計調整機構とその光学系の開発” 、日本天文学会春季年会、埼玉大学、3 月、2013 、W15c

4. 叶 哲生、芝井 広、伊藤優佑、山本広大、佐々木彩奈、秋山直輝、住 貴宏、深川美里、會見有香子、桑田嘉大、小西美穂子、成田正直 “遠赤外線干渉計 FITE: 新長軽量平面鏡の開発” 、日本天文学会春季年会、埼玉大学、3 月、2013 、W16c

5. 片多修平、秋山直輝、芝井 広、叶 哲生、伊藤優佑、山本広大、佐々木彩奈、住 貴宏、深川美里、會見有香子、桑田嘉大、小西美穂子、成田正直 “FITE 用新放物面鏡調整機構の開発” 、日本天文学会春季年会、埼玉大学、3 月、2013 、W17c

6. 秋山直輝、芝井 広、伊藤優佑、叶 哲生、山本広大、佐々木彩奈、住 貴宏、深川美里、會見有香子、桑田嘉大、小西美穂子、成田正直 “FITE 用遠赤外線圧縮型 Ge:Ga 二次元アレイセンサの開発” 、日本天文学会春季年会、埼玉大学、3 月、2013 、W18c

7. 芝井 広、住 貴宏、深川美里、叶 哲生、幸山常仁、伊藤優佑、山本広大、會見有香子、金子有紀、くわ田嘉大、Dimitrios Kontopoulos 、小西美穂子、蔡 承亨、佐々木彩奈、秋山直輝、白井皓寅、加藤恵理、成田正直、吉田哲也、斉藤芳隆、下浦美那、Antonio Mario Magalhaes 、Jose William Villas-Boas “気球搭載型遠赤外線干渉計 FITE：2010 年実験結果と次期フライト計画” 、日本天文学会春季年会、龍谷大学、3 月、2012 、W211c

8. 佐々木彩奈、芝井 広、住 貴宏、深川美里、叶 哲生、伊藤優佑、山本広大、會見有香子、金子有紀、くわ田嘉大、Dimitrios Kontopoulos 、蔡 承亨、秋山直輝、白井皓寅、成田正直 “WFS を用いた遠赤外線干渉計 FITE の光学調整方法の開発” 、日本天文学会春季年会、龍谷大学、3 月、2012 、W212b

9. 芝井 広、深川美里、加藤恵理、叶 哲生、幸山常仁、伊藤優佑、下浦美那、金子有紀、くわ田嘉大、川田光伸、渡部豊喜、中島亜紗美、山本広大、吉田哲也、斉藤芳隆、Antonio Mario Magalhaes, Jose Williams Vilas-Boas “気球搭載遠赤外線干渉計 FITE：初観測に向けて” 、日本天文学会春季年会、広島大学、3 月、2010 、W77b